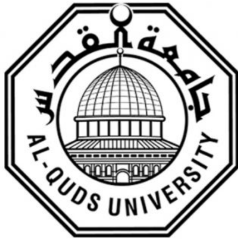

Palestine Polytechnic University

Deanship of Graduate Studies and Scientific Research

Master Program of Renewable Energy and Sustainability

Raman Spectroscopy for Analysis of Silicon Precursor Layers for Liquid Phase Crystallized Solar Cells

---

By

Suheir J. D. Nofal

Supervisors

Dr. Othman Zalloum, Palestine Polytechnic University

Dr. Maurice Nuys, Forschungszentrum Jülich, IEK-5

Thesis submitted in partial fulfillment of requirements of the degree

Master of Science in Renewable Energy Sustainability

March 2019

The undersigned hereby certify that they have read, examined and recommended to the Deanship of Graduate Studies and Scientific Research at Palestine Polytechnic University and the Faculty of Science at Al-Quds University the approval of a thesis entitled:

Raman Spectroscopy for Analysis of Silicon Precursor Layers for Liquid Phase Crystallized Solar Cells

Submitted by:

Suheir J. D. Nofal

in partial fulfillment of the requirements for the degree of Master in Renewable Energy Sustainability.

Graduate Advisory Committee:

Prof./Dr. ____________________

Signature: ____________ Date: ____________

Prof./Dr. ____________________

Signature: ____________ Date: ____________

Prof./Dr. ____________________

Signature: ____________ Date: ____________

Thesis Approved by:

Name: ____________	Name: ____________
Dean of Graduate Studies Palestine Polytechnic University Signature: ____________	Dean of Faculty of Graduate Studies Al-Quds University Signature: ____________
Date: ____________	Date: ____________

Raman Spectroscopy for Analysis of Silicon Precursor Layers for Liquid Phase Crystallized Solar Cells

By:

Suheir J. D. Nofal

Abstract

Amorphous silicon thin films based solar cells have a low efficiency comparing to the conventional poly-crystalline silicon wafer based solar cells. To overcome the efficiency limitation, the attempt to crystallize the amorphous silicon thin layers deposited by Plasma enhanced chemical vapor deposition (PECVD) on glass is investigated. the crystallization process is based on zone-melting technology and called liquid phase crystallization (LPC). Raman spectroscopy is used to analyze the properties of the silicon thin layers that is deposited by PECVD process and crystallized by LPC process; for better understanding of these processes. The present thesis provides the possibility of engaging Raman spectroscopy as a characterization method with MATLAB software as the analysis tool to investigate the properties of thin silicon precursor layers for liquid phase crystallized solar cells. The exported data after analysis has been plotted into two different categories; depth profiling as well as two-dimensional mapping. The first category includes three samples deposited on glass by plasma enhanced chemical vapour deposition with different deposition parameters (e.g.: silane concentration, rf power, and pressure) to investigate the influence of these parameters on having amorphous or micro-crystalline structure, as well as hydrogen content and micro-structure parameters. The first sample has a μc-Si structure with crystallinity changing with depth. The other two samples have a-Si structures. All samples have nearly a constant hydrogen content and micro-structure parameters with depth. Then, the amorphous samples have been annealed to investigate the influence of annealing on the structural order and hydrogen diffusion. The first one is thermally unstable, only 0.50 μm remains on glass after annealing. While the other is stable and the whole thickness remains unchanged during annealing. All hydrogen has been diffused in both samples. Raman spectroscopy is a useful technique to create

data that can be plotted as depth profiles for the crystallinity, structural order, hydrogen content, and micro-structure parameters for PECVD deposited precursors; hence gives a better understanding of the changes in these properties with depth. PECVD parameters of the last sample (SiH_4 flow rate of 6 sccm, H_2 flow rate of 12 sccm, pressure of 1 mbar, rf power of 25 W, and heater temperature of 450 ^oC) have been taken as the standard, since they deposit an a-Si structure, that is thermally stable after annealing among all samples. The second section includes one sample, which has been deposited by electron beam deposition, cut into five small samples, and then crystallized by liquid phase crystallization with different crystallization parameters (e.g.: laser scan speed and power) to investigate the influence of these parameters on stress inside the crystallized precursors. Three 2D maps have been taken in grain boundaries, where c-Si peak is shifting to lower wavenumbers; hence a tensile stress behavior along grain boundaries is mapped. Two 2D maps have been taken in the middle of a crack, where the stress behavior is varied between a tensile stress on one side of the crack and a compressive stress on the other side. The last 2D maps have been taken at a crack tip, where the crack starts at the surface but does not continue with depth. higher tensile stress has been mapped from the glass side, which does not reach its threshold value to form the crack yet. Raman spectroscopy is a helpful tool in investigate the stress resulted in LPC-Si precursors for better understanding of LPC process. LPC parameters of the first sample (red laser beam of 808 nm wavelength, substrate temperature of 510 ^oC, laser speed of 1 mm/s, and power of 45 W) have been taken as the standard, since they produce a non-cracked precursor with minimum number of grain boundaries among all samples.

استخدام طريقة تحليل طيف رامان في تحديد خصائص الطبقات الرقيقة من السيليكون المتبلورة في الطور السائل للخلايا الشمسية

سهير نوفل

الملخص :

تمتلك خلايا رقائق السيليكون الشمسية فاعلية أقل من الخلايا الشمسية التقليدية، لذلك فإن فكرة تحويل الرقائق اللابلورية إلى رقائق متبلورة على الزجاج يمكن أن يزيد من فاعليتها و تسمى هذه العملية تبلور الطور السائل. توفر هذه الأطروحة إمكانية الربط بين طريقة تحليل طيف رامان كطريقة توصيف مع برنامج ماتلاب كأداة لفحص خصائص طبقات السليكون الرقيقة للخلايا الشمسية المتبلورة في الطور السائل. تم رسم البيانات التي تم تصديرها بعد التحليل إلى قسمين مختلفين، القسم الأول علة شكل مخططات خطية أما الثاني فعلى شكل خرائط ثنائية الأبعاد. يتضمن القسم الأول ثلاث عينات مودعة على الزجاج بواسطة ترسيب بخار كيميائي معزّز بالبلازما باستخدام عوامل ترسيب مختلفة (على سبيل المثال: تركيز السيلان، الحرارة، الطاقة، والضغط) لدراسة تأثير هذه العوامل على وجود بنية غير بلورية أو بلورية من القياس المصغر، بالإضافة إلى محتوى الهيدروجين ومعلمات البنية الدقيقة. العينة الأولى لها بنية **μc-Si** مع تبلور متغيرة مع العمق. والعينتان الأخريان لهما هياكل غير متبلورة. تحتوي جميع العينات على محتوى هيدروجين ثابت ومعلمات بنية دقيقة مع العمق. بعد ذلك، تم شيّ العينات اللابلورية للتحقيق في تأثير الشيّ على الترتيب الهيكلي وخروج الهيدروجين من العينات. العينة الأولى كانت غير مستقر حرارياً ، فقط 0.50 ميكرومتر تبقت على الزجاج بعد الشيّ. في حين أن الأخرى كانت مستقرة حرارياً حيث أن كامل السماكة تبقت دون تغيير أثناء الشيّ. وقد تم خروج جميع الهيدروجين في كلتا العينات. يعتبر طيف رامان تقنية مفيدة للحصول على المعلومات التي يمكن رسمها كمخططات عمق للترتيب الهيكلي ومحتوى الهيدروجين، ومعلمات البنية الدقيقة لرقائق السيليكون المودعة بالبلازما؛ وبالتالي يعطي فهم أفضل للتغيرات في هذه الخصائص مع العمق. تم أخذ عوامل الترسيب من العينة الأخيرة كمعيار لعمليات الترسيب القادمة، لأنها تودع رقائق سيليكون ببنية غير متبلورة، كذلك مستقرة حرارياً بعد الشي من بين جميع العينات. يتضمن القسم الثاني عينة واحدة، تم ترسيبها بواسطة ترسيب الحزمة الإلكترونية ، وقطعها إلى خمس عينات صغيرة، تم تبلورت بواسطة تبلور الطور السائل بعوامل تبلور مختلفة (مثل: سرعة المسح الضوئي بالليزر والطاقة) للتحقق من تأثير هذه العوامل على الإجهاد داخل رقائق السيليكون المتبلورة. تم أخذ ثلاث خرائط ثنائية الأبعاد على حدود بين حبيبات الكريستال المتبلورة، حيث يتحرك طيف رامان لطول موجي منخفض اقل من 520 سم$^{-1}$. وبالتالي يتم تعيين سلوك التوتر على أنه شد على طول الحدود. تم أخذ خريطتين ثنائي الأبعاد في منتصف الصدع، حيث يختلف سلوك الإجهاد بين إجهاد الشد على أحد جانبي الصدع إجهاد الضغط على الجانب الآخر. تم أخذ آخر خريطة ثنائية الأبعاد عند طرف الصدع ، حيث يبدأ الكسر عند السطح ولكنه لا يستمر بالعمق. وقد تم تعيين إجهاد الشد الأعلى من الجانب الزجاجي ، والذي لا يصل إلى قيمة عتبة لتشكيل الصدع بعد حتى الآن. طيف رامان هو أداة مفيدة في التحقق من الإجهاد الذي نتج عنه تبلور السيليكون من أجل فهم أفضل لعملية التبلور. تم أخذ العوامل من العينة الأولى كمعيار لعمليات التبلور القادمة، لأنها تنتج رقائق غير متصدعة بين جميع العينات.

Declaration of Authorship

I declare that the Master Thesis entitled Raman Spectroscopy for Analysis of Silicon Precursor Layers for Liquid Phase Crystallized Solar Cells is my own original work, and herby certify that unless stated, all work contained within this thesis is my own independent research and has not been submitted for the award of any other degree at any institution, except where due acknowledgement is made in the text.

Student Name: ______________________________

Signature: ______________ Date: ______________

STATEMENT OF PERMISSION TO USE

In presenting this thesis in partial fulfillment of the requirements for the joint Masters degree in Renewable Energy Sustainability at Palestine Polytechnic University and Al-Quds University, I agree that the library shall make it available to borrowers under rules of the library.

Brief quotations from this thesis are allowable without special permission, provided that accurate acknowledgement of the source is made.

Permission for extensive quotation from, reproduction, or publication of this thesis may be granted by my main supervisor, or in [his/her] absence, by the Dean of Graduate Studies and Scientific Research [or Dean of Faculty of Graduate Studies] when, in the opinion of either, the proposed use of the material is for scholarly purposes.

Any coping or use of the material in this thesis for financial gain shall not be allowed without my written permission.

Student Name: ______________________________

Signature: ______________ Date: ______________

To my family and friends who first believed I can . . .

"I've learned that fear limits you and your vision. It serves as blinders to what may be just a few steps down the road for you. The journey is valuable, but believing in your talents, your abilities, and your self-worth can empower you to walk down an even brighter path. Transforming fear into freedom - how great is that?"

Soledad O'Brien

Acknowledgement

I would like to thank JAMILA Project-544339-TEMPUS-1-2013-1-IT-TEMPUS-JPCR funded by the European Union which was administrated by Sapienza University of Rome and partner Universities for their support in launching this program, provided infrastructure and opportunities for scientific visits.

The present Master thesis is part of the framework of Palestinian German Science Bridge (PGSB), which is a pilot project financed by the German Federal Ministry of Education and Research (BMBF) and implemented jointly by Forschungszentrum Jülich GmbH (FZJ) and Palestinian Academy for Science and Technology (PALAST).

I would like to thank Dr. Othman Zalloum and Prof. Uwe Rau for giving me the opportunity to do my MSc thesis at IEK-5. Dr. Maurice Nuys for his patient guidance, encouragement and advice throughout my time in Jülich. Dr. Stefan Haas for his invaluable guidance and suggestions. Hassan Ali for preparing the samples for the experiments. Markus Hülsbeck for his technical support and help with Raman setups. Gunnar Schöpe and Andreas Bauer for laser processing. Brigitte Zwaygardt for etching. Pascal Foucart for AFM images. Sina Kurth and Aryak Singh for their kind help and support. I have been extremely lucky to work with all of you.

Symbols

Å	Ångstrom
$ARcoating$	Anti-Reflective coating
$ASCII$	American Standard Code for Information Interchange
$a - Si$	amorphous Silicon
$a - Si : H$	Hydrogenated amorphous Silicon
CCD	Charge Coupled Device
$c - Si$	Crystalline Silicon
d	distance
D	Dipole moment
E	Electric field
$FWHM$	Full Width at Half Maximum
h	Depth
I_{RA}	Raman Intensity
k	Raman Shift
KOH	Potassium Hydroxide
HF	Hydrofluoric Acid
$HWCVD$	Hot Wire Chemical Vapour Deposition
μc-Si	Micro-crystalline Silicon
$PECVD$	Plasma Enhanced Chemical Vapour Deposition
EB	Electron Beam Deposition
LA	Longitudinal Acoustic Mode
$LASER$	Light Amplification by Simulated Emission of Radiation
LPC	Liquid Phase Crystallization
LO	Longitudinal Optic Mode
LRO	Long Range Order
Q	normal coordinate of the vibration
R_{SiH}	Micro-structure Parameters

rf	Radio Frequency
$MATLAB$	MATrix LABoratory
MRO	Medium Range Order
SC	Silane Concentration
SiH_4	Monosilane
SiO_2	Silicon Dioxide
SRO	Short Range Order
T	Temperature
TA	Transversal Acoustic Mode
TO	Transversal Optic Mode
X_c	Crystallinity

α	Absorption Coefficient
α_i	Polarizability of the molecule
ω_{TO}	Width of TO peak centered at $480\,\mathrm{cm}^{-1}$
θ	SRO

List of Figures

2.1 Schematic image of PECVD chamber 5
2.2 Schematic image of the laser LPC process 6
2.3 Schematic image of light scattering cases 7
2.4 Schematic image of a) a-Si structure b) c-Si structure 8
2.5 Typical Raman spectrum of an in a-Si structure 9
2.6 Typical Raman spectrum of a c-Si structure 10
2.7 Raman spectra of TO mode of a c-Si structure 10
2.8 Schematic image of μc-Si structure 11
2.9 Typical Raman spectrum of a μc-Si structure 12
2.10 Schematic image of a-Si:H structure 12
2.11 Typical Raman spectrum for Si-H vibrational modes 13
2.12 Schematic image of single monochromatic Raman Setup. 14
2.13 Schematic image of double monochromatic Raman Setup. 14

3.1 a) Microscopic image of the edge of a crater b) Depth profile of the sidewall scanned by Dektak profilometer 18
3.2 Raw data produced from a single monochromatic Raman setup . . . 19
3.3 Schematic image of the sample layout 21

4.1 Baseline fitting for a Raman spectrum 24
4.2 Final spectrum after normalization 25
4.3 Rama spectrum for Si-Si vibrational phonon modes region in a-Si structure 26

5.1 Raman spectra of the μc-Si sample 29
5.2 Depth profile of of crystallinity for μc-Si structure 29
5.3 Raman spectra of Si-H vibrational phonon modes for μc-Si structure 30
5.4 Depth profile of a) hydrogen content b) microstructure parameters . 30
5.5 a) Raman spectra of the unstable a-Si sample before annealing b) Raman spectra of the stable a-Si sample before annealing 32
5.6 Depth profile of a) Medium range order b) Short range order for the a-Si samples before annealing 32
5.7 a) Raman spectra of Si-H bonds for the unstable a-Si sample before annealing b) Raman spectra of Si-H bonds for the stable a-Si sample before annealing 33
5.8 Depth profile of a) Hydrogen content b) Microstructure parameter for the unstable sample before annealing 33

5.9 Depth profile of a) Hydrogen content b) Microstructure parameter for the stable sample before annealing 34
5.10 Raman spectra of vibrational phonon modes for the unstable sample after annealing 35
5.11 Depth profile of a) Medium range order b) Short range order for the unstable sample before and after annealing 35
5.12 Raman Spectra for Si-H vibrational phonon modes for the unstable after annealing 36
5.13 Depth profile of hydrogen content for the unstable sample after annealing 36
5.14 Raman spectra of vibrational phonon modes for the stable sample after annealing 37
5.15 Depth profile of a) Medium range order b) Short range order for the stable sample before and after annealing 37
5.16 Raman spectra for Si-H vibrational phonon modes for the stable after annealing 38
5.17 Depth profile of hydrogen content for the stable sample after annealing 38
5.18 a) Microscopic image b) 2D map of Raman shift and stress for a stress free area. 40
5.19 a) Microscopic image b) 2D map of Raman shift and stress for an area around a grain boundary 41
5.20 a) Microscopic image b) 2D map of Raman shift and stress for an area around a grain boundary 41
5.21 a) Microscopic image b) 2D map of Raman shift and stress for an area around a grain boundary from surface side 42
5.22 a) Microscopic image b) 2D map of Raman shift and stress for an area around a grain boundary from glass side 42
5.23 Microscopic image for the selected areas for Raman measurement . 43
5.24 a) Microscopic image b) 2D map of Raman shift and stress for a cracked area 44
5.25 a) Microscopic image b) 2D map of Raman shift and stress for a cracked area from the surface side 46
5.26 a) Microscopic image b) 2D map of Raman shift and stress for a cracked area form glass side 46
5.27 a) Microscopic image b) 2D map of Raman shift and stress for a crack tip form the surface side 47
5.28 2D map of Raman shift and stress for a crack tip form glass Side . . 47

6.1 Process sequence of silicon thin film based solar cell fabrication. . . 52

List of Tables

3.1 PECVD deposition parameter summary 16
3.2 Laser LPC Parameters Summary 20

Contents

Symbols **x**

List of Figures **xii**

List of Tables **xiv**

1 Introduction **1**

2 Fundamentals and Basics **4**
- 2.1 Plasma Enhanced Chemical Vapour Deposition 4
- 2.2 Liquid Phase Crystallization 5
- 2.3 Raman Spectroscopy 6
- 2.4 Raman Spectra for Silicon Structures 8
- 2.5 Raman Spectrum for Hydrogenated Structure 12
- 2.6 Raman Setup 13

3 Experiments **15**
- 3.1 Substrate Preparation 15
- 3.2 Raman Measurement for Depth Profiling 16
  - 3.2.1 Samples Preparation 16
  - 3.2.2 Potassium Hydroxide Etching 17
  - 3.2.3 Dektak Profilometer 17
  - 3.2.4 Measuring Raman Spectra 18
- 3.3 Raman Measurement for 2D Mapping 20
  - 3.3.1 Samples Preparation 20
  - 3.3.2 Hydrofluoric Acid Etching 21
  - 3.3.3 Measuring Raman Spectra 21

4 MATLAB for Data Analysis and Calculations **23**
- 4.1 Raman Measurement for Depth Profiling 23
  - 4.1.1 Baseline Fitting 23

4.1.2 Normalization 24
4.1.3 Peaks Fitting and Calculations 25
4.2 Raman Measurement for 2D Mapping 27
4.2.1 Data Import 27
4.2.2 Peaks Fitting and Calculations 27
4.2.3 Cracks Identification 27

5 Results and Discussion **28**
5.1 Raman Measurement for Depth Profiling 28
5.1.1 Analysis of μc-Si:H 28
5.1.2 Analysis of a-Si:H Before Annealing 31
5.1.3 Analysis of a-Si:H After Annealing 34
5.2 Raman Measurement for 2D Mapping 39
5.2.1 Non Stressed Areas 39
5.2.2 Grain Boundaries Areas 40
5.2.3 Cracked Areas 43

6 Summary and Outlook **48**

A An Appendix **53**
A.1 baseline Fitting 53
A.2 baseline Fitting 54
A.3 Example of Depth Profiling 55
A.4 Example of 2D mapping 56

Bibliography **57**

Chapter 1

Introduction

Solar cells have been well known as one of the renewable resources in the energy industry for a long time. According to the Photovoltaic Report 2018, the annual growth rate of solar cells installation reached 24 % between 2010 and 2017. Monocrystalline silicon wafer based solar cell is the most extensively researched solar cell technology in the energy market, with a share of 93 % of total solar cells in 2017. These solar cells recorded a lab efficiency of 26.7 %.[1] Despite the fast growth of these solar cells, their production cost remains rather high. To overcome this limitation, thinner layers of silicon (about 10 % of wafer's thickness) have been proposed to be deposited on low-cost glass substrates via gas phase. Solar cells based on this concept are called thin film based solar cells [2, 3].

Thin silicon film based solar cells are known as part of the so-called second generation of solar cells, where thin silicon layers (e.g.: amorphous (a-Si:H), microcrystalline (μc-Si:H)) are deposited on glass by Plasma Enhanced Chemical Vapor Deposition [2], Hot Wire Chemical Vapor Deposition and other techniques, in a thickness ranges between (5-20) μm. These thin silicon film based solar cells have a very low production cost, but also have much lower efficiency (around 11 %) than silicon wafer based solar cells. Hence their total share in the PV market remains only around 5 %.[1] To overcome the efficiency limitation and make thin solar cells more competitive to conventional silicon wafers; the attempt to crystallize thin silicon layers and have poly-crystalline silicon thin films looks very promising, known as liquid phase crystallization (LPC) [4, 5].

Liquid phase crystallization have a high potential to produce large-grains silicon layer on cheap glass by using an energy source. This process depends on zone-melting technology. In 1960s, zone melting technology was investigated for the growth of low-melting point semiconductors such as Ge, but failed with silicon. [4] The interest in this technology renewed lately by different research groups in the field of photovoltaics in Germany [5–7] and Australia [8]. The idea was first introduced by Helmholtz-zentrum Berlin in 2009 [5]. The work on this technology is done jointly between Helmholtz-zentrum Berlin and Forschungszentrum Jülich GmbH. Past investigation has been done to select the glass substrate as well as the design of the intermediate layer [3, 9]. Further investigations are still ongoing to select the deposition technique and LPC process that will give high quality poly-crystalline silicon on glass, and increase the open circuit voltage and efficiency [5].

In the Institute of Energy and Climate Research Photovoltaics (IEK-5) at Forschungszentrum Jülich GmbH, the research group Laser Processes and Module Technology is working to modify and optimize material properties of all layers used in typical thin silicon film based solar cells, also to investigate and optimize the required laser processes e.g. the selective laser ablation of the front contact, absorber and back contact. One of the group's goals is to investigate the possibility of producing poly-crystalline silicon precursors by liquid phase crystallization; to improve the film's crystallinity. [6]

The main focus of the present thesis is to develop different techniques using Raman spectroscopy as a characterization method and MATLAB software as the analysis tool to gain detailed information about the properties of the precursors before and after crystallization. This thesis is divided into two sections, the first section deals with the investigation of properties of amorphous and micro-crystalline silicon layers after PECVD deposition and before crystallization. While the other section concerns with the investigation of properties of crystallized silicon layers after the crystallization process.

Chapter 2 briefly introduces the basic knowledge about plasma enhanced chemical vapor deposition, liquid phase crystallization, silicon structures, and Raman spectroscopy. Chapter 3 describes the preparation process of the two different sets of samples and the methods used for measuring Raman spectra in the lab for both. Chapter 4 presents the data analysis procedure and calculations that have been taken by MATLAB software for both sections. Chapter 5 introduces and discusses

the results coming out from the different samples. Finally, chapter 6 summarizes the main results of this thesis.

Chapter 2

Fundamentals and Basics

In this chapter, plasma enhanced chemical vapour deposition (PECVD), liquid phase crystallization process (LPC), and Raman spectroscopy are introduced in detail. The different silicon structures are also presented.

2.1 Plasma Enhanced Chemical Vapour Deposition

Plasma enhanced chemical vapour deposition (PECVD) is used to deposit thin silicon layers (e.g.: amorphous (a-Si:H) and micro-crystalline (μc-Si:H)) on glass by chemical reactions initiated by high energy plasma. Chemical vapour deposition was first introduced in the mid-60s and developed very fast over the years. [10] More literature about CVD in general, and PECVD in particular can be found in [10].

Figure 2.1 shows a schematic of a PECVD chamber. The chamber has two parallel electrodes; one is grounded while the other is connected to a radio frequency generator. The glass is placed on the grounded electrode, which is also connected to a heater. Mono-silane gas (SiH_4) is mixed with hydrogen gas (H_2) before folwing into the chamber between the two electrodes. The coupling excites the mixed gases into a high energy plasma by the radio frequency power, and the reaction products (Si, SiH, SiH_2, and SiH_3) diffuse towards the glass substrate to form a thin layer. [2, 10]

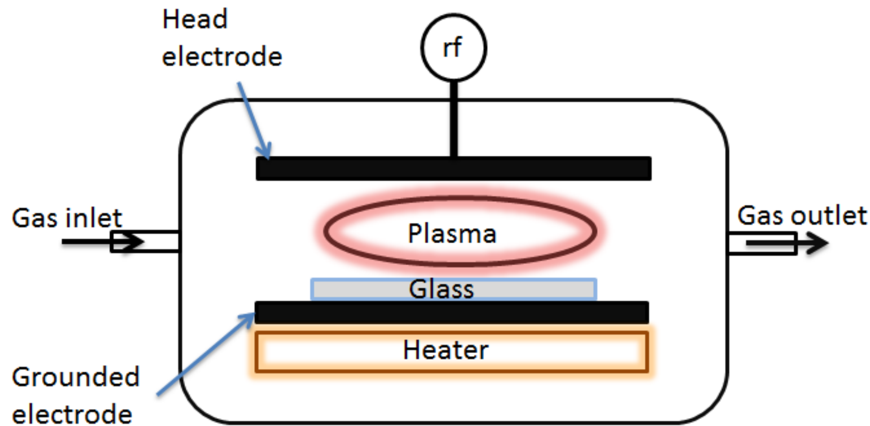

FIGURE 2.1: Schematic image of PECVD chamber. The chamber has two electrodes, one is connected to rf generator while the other is grounded and connected to a heater, the glass is placed on the grounded electrode.

2.2 Liquid Phase Crystallization

Liquid phase crystallization (LPC) is based on zone-melting technology; in which, rapid melting of silicon (e.g.: amorphous or micro-crystalline) is introduced to produce high-quality poly-crystalline silicon layers directly on glass by using an electron or a laser beam. Figure 2.2 shows a schematic image of the laser LPC process. A line-shaped continuous wave laser beam is focused on the thin film and used as a heat source to crystallize the thin layer and produce a poly-crystalline silicon layer on glass. [3, 4, 9]

The laser beam with a suitable wavelength starts scanning the sample and locally melts the silicon. Silicon cools down below the melting point and solidifies rapidly after the laser moves away. The nucleation of small grains starts, which grow laterally in the same direction of the scanning laser beam. Grains can reach a size of millimeters or centimeters in some cases after the crystallization. Their sizes depend on the selected laser scan speed and power, which should be high enough to produces grains; but also low enough to prevent crack formation. [3, 4, 9, 11]

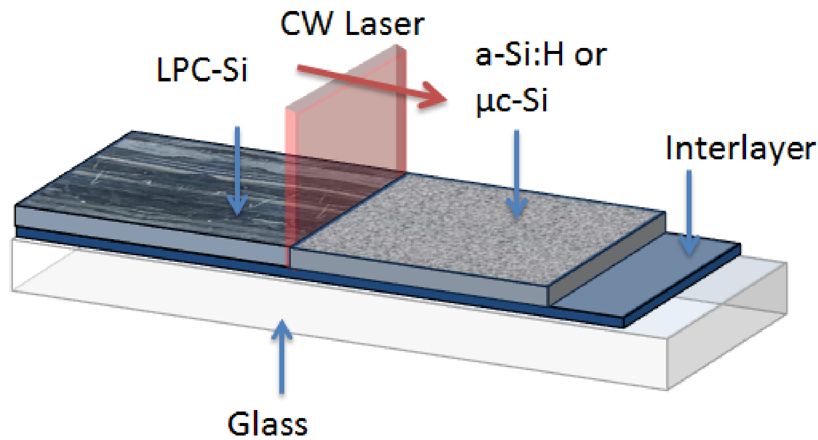

FIGURE 2.2: Schematic image of LPC process after J. Haschke et al. 2016 [9]. A laser beam is focused on a thin film to melt the silicon layer (a-Si or μc-Si) on glass, and produce ploy c-Si structure.

2.3 Raman Spectroscopy

Raman spectroscopy is a non-destructive spectroscopic method, based on the inelastic scattering of monochromatic light. It is used to investigate vibrational phonon modes of matters. It was first demonstrated by the Indian scientist Sir C.V. Raman, who observed the effect on an organic liquid by the mean of sunlight experimentally. More literature can be found in [2, 12].

Figure 2.3 shows the schematic image of the three possible cases of light scattering. When a monochromatic incident light interacts with a material, the largest part of the light is scattered elastically without any energy exchange between the light and the electron, and the scattered photon has the same wavelength as before scattering. This interaction is known as Rayleigh scattering. However, a very small fraction of the incident light scatters inelastically. The scattered light can have a higher or lower wavelength according to the initial state of the electron. This phenomenon is well known as Raman effect. [12, 13]

By this energy exchange, a phonon is excited or annihilated. If the scattered light has lower energy than the incident light, a phonon is excited and known as Stokes shift. By contrast, if the scattered light has higher energy, a phonon is annihilated and known as Anti-Stokes shift. The frequency shift between the incident and scattered lights is called Raman shift k and measured in relative wavenumber. [2, 12]

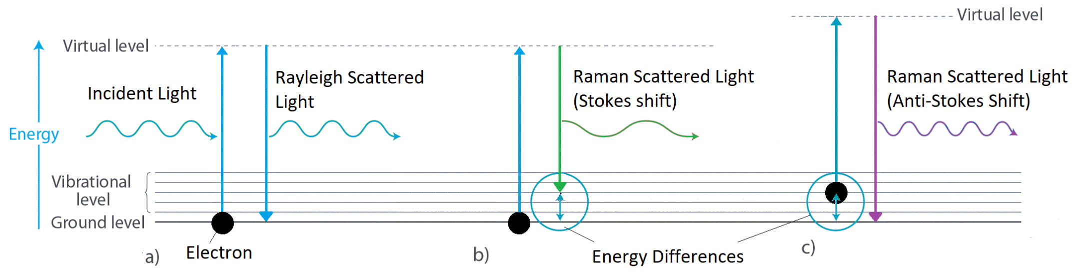

FIGURE 2.3: Schematic image of light scattering cases after Nanophoton 2016 [12]. a) Rayleigh scattering: No energy exchange b) Stokes shift: A phonon is excited c) Anti-stokes shift: A phonon is annihilated.

The vibrational spectrum of a molecule is composed of bands representing some active normal vibrations. The spectrum depends on the masses of the atoms in the molecule, the strength of their chemical bands and the atomic arrangement. Crystal lattice vibrations and other motions of extended solids are Raman-active. [14]

A simple classical electromagnetic field description of Raman spectroscopy can be used to explain the important features of Raman band intensities. The dipole moment (D) induced in a molecule by an external electric field (E) is proportional to the field [14], as in the following equation:

$$D = \alpha_i E \tag{2.1}$$

The proportionality constant (α_i) is the polarizability of the molecule. The polarizability measures the ease with which the electron cloud around a molecule can be distorted. The induced dipole emits or scatters light at the optical frequency of the incident light wave. Raman scattering occurs because a molecular vibration can change the polarizability. The change is described by the polarizability derivative ($\frac{d\alpha_i}{dQ}$), where Q is the normal coordinate of the vibration. [14] The selection rule for a Raman-active vibration is:

$$\frac{d\alpha_i}{dQ} \neq 0 \tag{2.2}$$

The Raman selection rule is analogous to the more familiar selection rule for an infrared-active vibration, which states that in order for a vibration to be Raman-active, there must be a change in polarizability during the vibration [12, 14].

The Raman spectrum is a unique fingerprint of matter, where a particular peak originates due to specific lattice vibration. [12] Raman spectra of different silicon structures and the difference between them are discussed in the following two sections.

2.4 Raman Spectra for Silicon Structures

Silicon atoms have a certain structural arrangement in the lattice space, but can be slightly different in the periodic order in long, medium, and short ranges between amorphous, crystalline, and micro-crystalline structure. This difference can be clearly visible in Raman spectra. Each structure has a unique Raman spectrum. In case of an amorphous silicon structure, the atoms are arranged in a tetrahedral structure with non-uniform bond angles between them. The atoms lose their periodic order in long range, as illustrated in figure 2.4 a). But still, a certain bond angle between neighbouring atoms remains in short and medium ranges. Short range order (SRO) has a length scale between (2-5) Å. Higher value leads to a higher order in SRO areas. Medium range order (MRO) has a length scale between (5-20) Å. It indicates how the tetrahedrons are twisted against each other. Note that in this case, not all of the silicon bonds are saturated leading to defect states within the band gap. These unsaturated bonds are known as dangling bonds. [15]

Figure 2.5 shows a typical Raman spectrum for a-Si structure for Si-Si bonds. Four

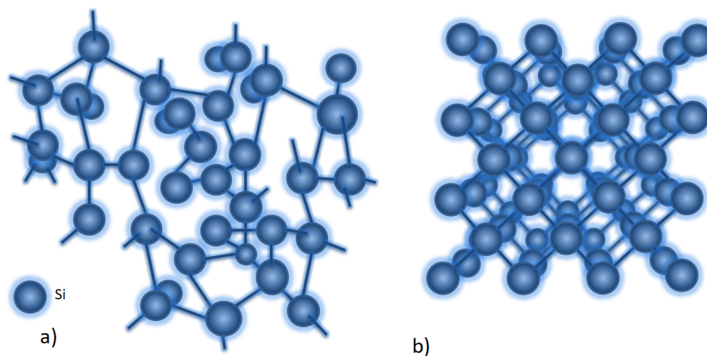

FIGURE 2.4: Schematic image of a) a-Si structure: Non-uniform length and bond angles between atoms b) c-Si structure: Uniform length and bond angles.

vibrational phonon [1]modes are Raman active in the region between 100 cm^{-1} and 600 cm^{-1}. The intensities of these modes can be used to correlate MRO, as in equation 2.3. [16, 17]

$$MRO = \frac{I_{TO}}{I_{TA}} \tag{2.3}$$

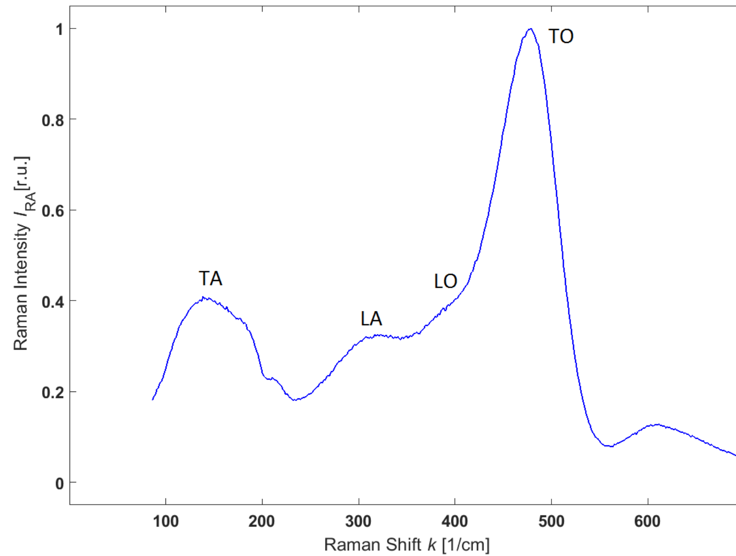

FIGURE 2.5: Typical Raman spectrum of an in a-Si structure. The four vibration modes (TO, LO, LA, and TA modes) are Raman active.

Where I_{TO} is the integrated intensity of TO mode centered at 480 cm^{-1} and I_{TA} is the integrated intensity of TA mode centered at 140 cm^{-1}. For SRO, the width of TO mode is only needed as in equation 2.4, where $\Delta\,\theta_B$ is SRO and ω_{TO} is the full width of the TO mode.[16, 17]

$$\Delta\theta = \frac{\omega_{TO} - 15}{6} \tag{2.4}$$

In case of crystalline silicon, the atoms have a diamond structure with two cubic face-centered unit cell, where uniform bond angles of 109.5$^{\,o}$ are noticed between atoms. The unit cell is repeated periodically in the long range, as illustrated in figure 2.4 b). [4] As in figure 2.6, a typical Raman spectrum of vibrational phonon modes for c-Si structure shows that TO mode is the only Raman active mode centered at 520 cm^{-1}.

[1]According to the phonon dispersion curve of silicon [16], four vibrational modes of a phonon are introduced, known as [TO mode: Transversal Optical mode, TA mode: Transversal Acoustics mode, LO mode:Longitudinal Optical mode, LA mode: Longitudinal Acoustics mode].

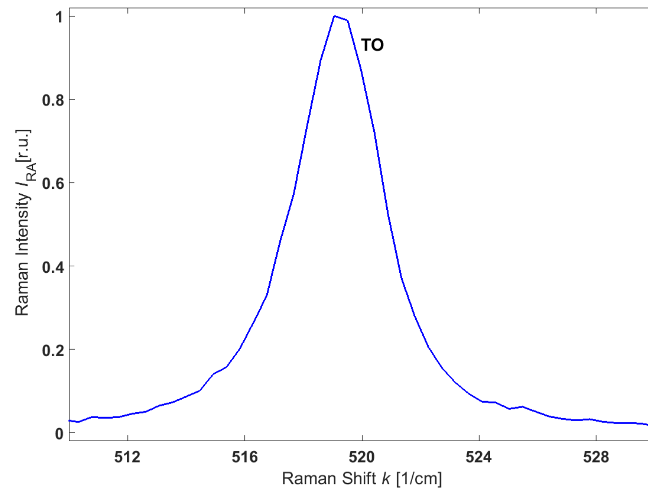

FIGURE 2.6: Typical Raman spectrum of a c-Si structure. TO mode is the only Raman active mode.

Stress leads to a shift of the TO mode away from 520 cm^{-1}. This method can be used to investigate stress inside the crystallized silicon materials. Equation 2.5 is used, where σ is the bi-axial stress in MPa and Δk is Raman shift difference in cm^{-1}. As illustrated in figure 2.7, a peaking shifts above 520 cm^{-1} indicates a compressive stress inside the structure, while a peak shifting below 520 cm^{-1} indicates a tensile stress. [12, 18, 19]

$$\sigma = 250 * (\Delta k) \tag{2.5}$$

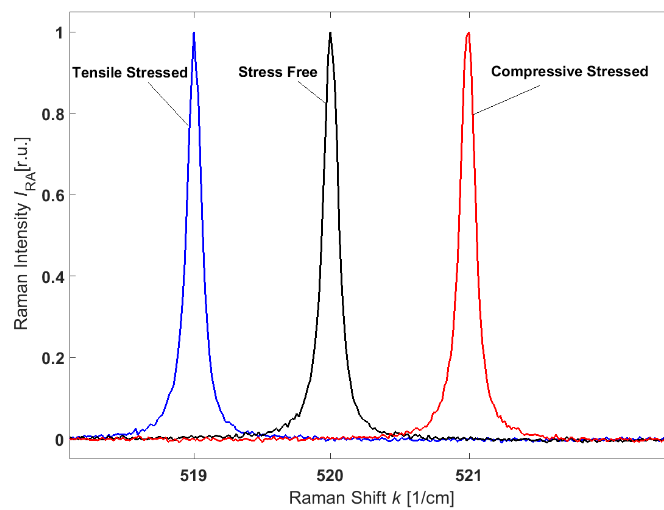

FIGURE 2.7: Raman spectra of TO mode of a c-Si structure. Higher Raman shift leads to compressive stress (red peak), while lower Raman shift leads to tensile stress (blue peak).

A mixture between amorphous and crystalline phases is known as micro-crystalline or nano-crystalline silicon structure. Figure 2.8 shows the transition between amorphous and crystalline phases. From right to left, the structure changes from fully amorphous to fully crystalline. In between, degree of crystallinity within the structure is increased in the same direction of the arrow. Composition can be gradually changed by changing the deposition parameters. [2, 17, 20]

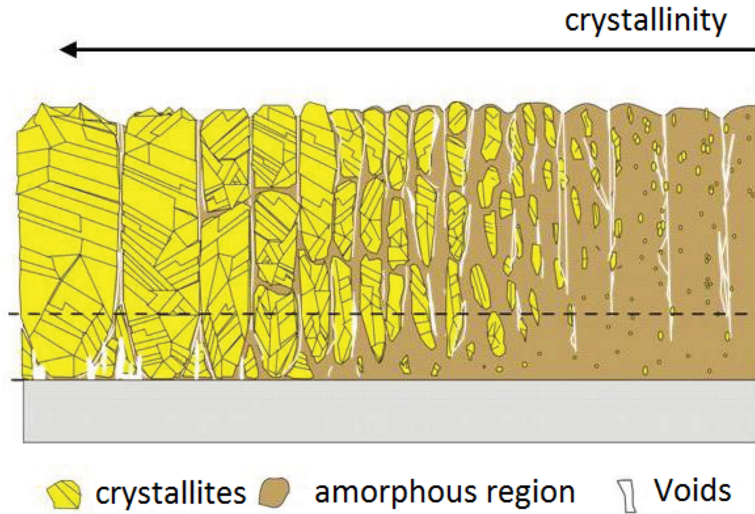

FIGURE 2.8: Schematic image of µc-Si structure [20]. From right to left, crystallinity changes from fully amorphous to fully crystalline structure, degree of crystallinity is increasing in the same direction of the arrow.

Figure 5.1 shows a typical Raman spectrum for a µc-Si structure, where TO mode is the only Raman Active mode, with a signal in the region between 400 cm^{-1} and 600 cm^{-1}. This signal can be fitted into three Gaussian peaks. To quantify the degree of crystallinity (X_c), equation 2.6 is used [21]. Where I_c is the integrated intensity for the crystalline phase centered at 516 cm^{-1} (not at 520 cm^{-1} like the fully crystalline structure), I_a is the integrated intensity for the amorphous phase centered at 480 cm^{-1}, and I_t is the integrated intensity for the transition phase between them centered at 500 cm^{-1}. [21]

$$X_c = \frac{I_c + I_t}{I_c + I_a + I_t} \tag{2.6}$$

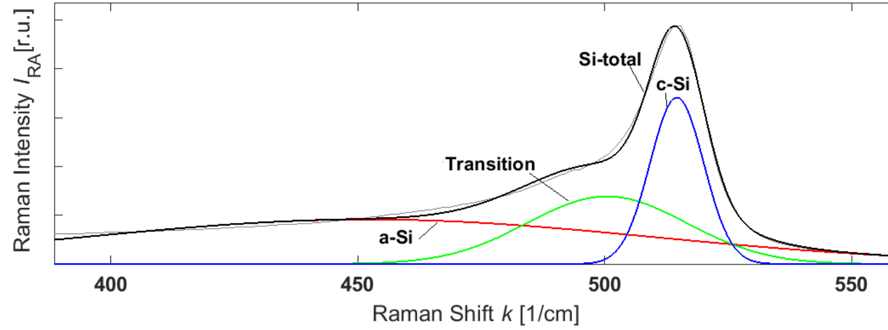

FIGURE 2.9: Typical Raman spectrum of a µc-Si structure. TO is the only Raman active mode, with a signal fitted into three Gaussian peaks; one for a-Si phase (green peak), the second for c-Si phase (blue peak), while the third for the transition phase between them (red peak).

2.5 Raman Spectrum for Hydrogenated Structure

Hydrogen and mono-silane are deliberately added in the gas mixture during the PECVD process. Therefore, hydrogen atoms are present in the resulted amorphous or micro-crystalline silicon structures. Hydrogen is necessary to saturate the dangling bonds and reduce the defect density in the resulted structure. The dangling bonds in silicon atoms are bonded with hydrogen atoms in either single bonds as Si-H or double bonds as Si-H_2, as illustrated in figure 2.10. Si-H bonds are correlated to compact a-Si:H structures, while Si-H_2 bonds are correlated to void rich a-Si:H structures. The relation between the two bonds (as in equation 2.7) is known as micro-structure parameters (R_{SiH}).[16, 22]

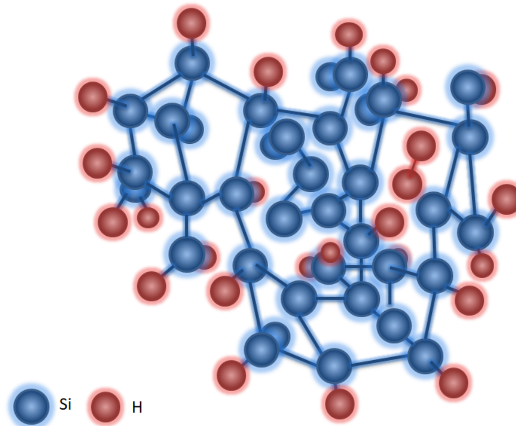

FIGURE 2.10: Schematic image of a-Si:H structure. dangling bonds are bonded to one or two atoms of hydrogen, dangling bonds are saturated with hydrogen atoms.

Figure 2.11 shows a typical Raman spectrum for Si-H vibrational phonon modes in the region between 1850 cm^{-1} and 2250 cm^{-1}. To quantify R$_{SiH}$, equation 2.7 is used, where I_{H2000} is the integrated intensity of Si-H phonon mode centered at 2000 cm^{-1} and I_{H2100} is the integrated intensity of Si-H$_2$ phonon mode centered at 2100 cm^{-1}. [15, 23]

$$R_{SiH} = \frac{I_{H2100}}{I_{H2000} + I_{H2100}} \tag{2.7}$$

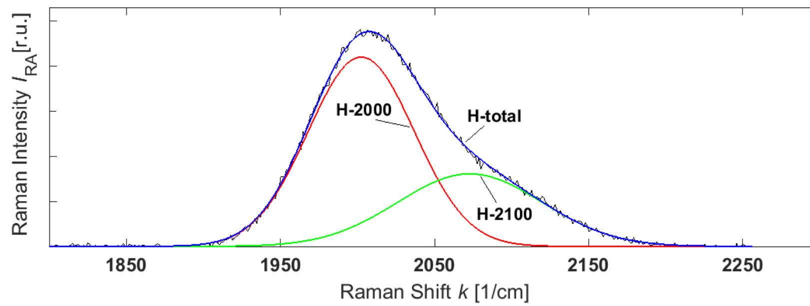

FIGURE 2.11: Typical Raman spectrum for Si-H vibrational modes in both a-Si:H and µc-Si:H structures. The signal is fitted into two Gaussian peaks, one for Si-H at 2000 cm^{-1} (red peak), the second for Si-H$_2$ at 2100 cm^{-1} (green peak).

2.6 Raman Setup

As illustrated in figure 2.12, a typical single monochromatic Raman setup has a laser source, a microscope, a single grating monochromator, and a detector. A camera is also attached to the microscope for optical observation. The Raman microscope has lenses of different objectives to focus the laser source on the sample. Once the sample is illuminated, some of the light is scattered back. This scattered light passes through the objective into two edge filters to reduce the scattered light by a factor of 10^{12}; so it does not damage the detector. The monochromator has a grating with a groove density of 1800 mm^{-1} which is used to disperse the scattered light. Finally, the monochromator is attached to a silicon-CCD detector.[13] The detailed parameters and the experimental procedure using this setup are discussed in section 3.2.

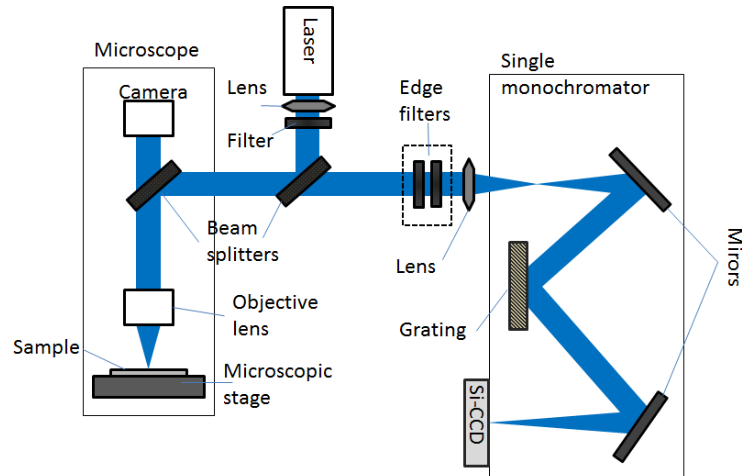

FIGURE 2.12: Schematic image of single monochromatic Raman Setup. A blue laser hits the sample and scatters, then filters by two edge filters before entering a monochromator, where the light is dispersed by a grating, then detected by Si-CCD camera

Figure 2.13 shows a schematic image of the double monochromatic Raman setup. The setup has the same configuration as the single monochromatic; the only difference is that the monochromator has two gratings. The scattered light is passed through the two gratings in series, so it is dispersed more to have a higher resolution signal. The detailed parameters and the experimental procedure using this setup are discussed in section 3.3.

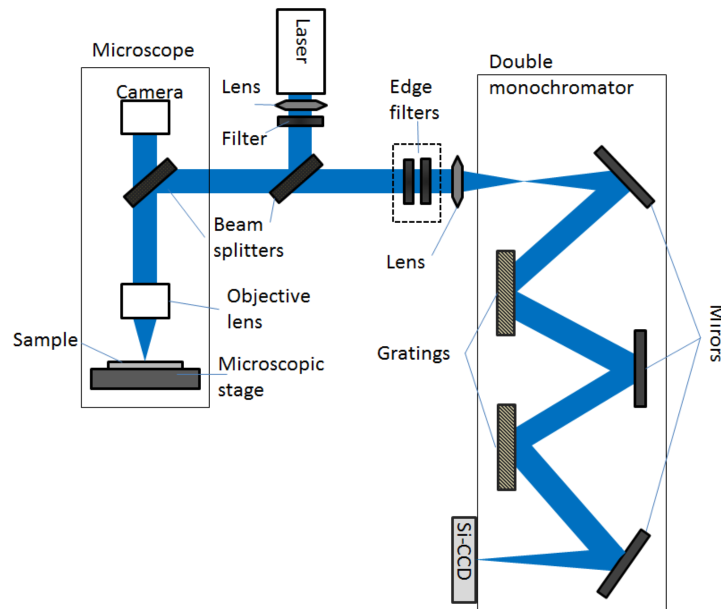

FIGURE 2.13: Schematic image of double monochromatic Raman Setup. Two gratings are installed in series to disperse the scattered light twice.

Chapter 3

Experiments

In this thesis, two different sets of samples have been investigated by Raman spectroscopy. The first set of samples before crystallization has been used for depth profiling, while the second set after crystallization has been used for two dimensional mapping. In this chapter, the complete process including samples preparation and measuring Raman spectra are presented in detail.

3.1 Substrate Preparation

Samples on both sets were fabricated on 1.1 mm Corning Eagle XG substrate [24]. It was chosen since its thermal expansion matches the thermal expansion of silicon. Next, an inter-mediated layer was deposited on glass. This layer acts as a diffusion barrier since the impurities from the glass can diffuse into the silicon layer during the crystallization. A sequence of 200 nm SiO_2/ 80 nm$SiNx$/200 nmSiO_2 was deposited by PECVD on top of glass, then annealed to diffuse all hydrogen out. Note that past experiments were done to have the best sequence for this layer, which is not within the context of this thesis.

3.2 Raman Measurement for Depth Profiling

3.2.1 Samples Preparation

For the first set, three 2x2 cm^2 sized samples have been prepared using PECVD technique with different deposition conditions (e.g. silane concentration, radio frequency (rf) power, and pressure). These parameters are summarized in Table 3.1. Variation of these parameters influences the micro-structure of the films (e.g. amorphous or micro-crystalline).

The first sample has a μc-Si:H layer with a thickness of 2 μm, while the other two samples have a-Si layer with 4.5 μm thickness each. The heater has been set at 450 ^{o}C for all depositions. Structural order, Hydrogen content, and micro-structure parameters have been investigated by Raman spectroscopy for these samples.

TABLE 3.1: PECVD deposition process summary

Sample Number	SiH_4 flow rate [sccm]	H_2 flow rate [sccm]	Silane Concentration SC [%]	Pressure p [mbar]	rf Power P [W]
1	12	60	83	0.50	90
2	12	228	95	6	90
3	6	12	66.66	1	25

Afterwards, an annealing step has been performed for the two amorphous samples by heating from room temperature to a temperature of 510 ^{o}C inside a high vacuumed chamber for 30 minutes, then letting them cool down for two hours before taking them out. The first amorphous sample is thermally unstable; only 0.50 μm of the material remains on glass after annealing. It is not yet clear why this thermal behaviour occurs in some samples, further investigation should be done in the future which is not within the context of this thesis. The other sample shows a stable behaviour in which the whole thickness remains unchanged during annealing. The influence of annealing on the structural order, hydrogen content, and micro-structure parameters have been similarly investigated for these samples using Raman spectroscopy.

3.2.2 Potassium Hydroxide Etching

Due to the low penetration depth of the blue laser in a-Si structures, wet chemical etching has been used to etch a crater into the samples. The etching process has been carried out with potassium hydroxide (KOH) with a concentration of 3 mol/L. During etching process, KOH reaction stops after some time; hence a fresh KOH solution must be introduced during the etching. Finally, the sample should be covered with a Petri dish the whole time to prevent water evaporation during the etching. [23, 25]

To create a crater on each sample, first a single drop of KOH has been placed on the surface and covered with the Petri dish for 10 minutes. Then, another KOH drop has been added. After another 10 minutes, a crater has been formed and the entire film has been etched until the glass substrate. The total time of 20 minutes has been good enough to etch all samples. The etching is done with the following reaction:

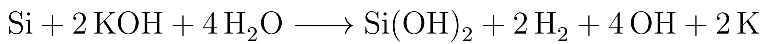

$$Si + 2\,KOH + 4\,H_2O \longrightarrow Si(OH)_2 + 2\,H_2 + 4\,OH + 2\,K$$

3.2.3 Dektak Profilometer

The crater created by KOH etching has been then measured by Dektak profilometer, which is a device with a tip of 12.5 µm in diameter. The tip moves along the surface to measure the topography of that surface. [26] It is important for Raman scan to have a sidewall that is smooth with neither holes nor steeps [23] over a horizontal length of more than 200 µm for a thickness between 2-4.50 µm (as shown in figure 3.1 b)) to have enough points on the sidewall.

To find the position of the sidewall again in the Raman microscope, the edge of the crater is marked with a nano-second laser of 1026 nm wavelength and 500 mW power, as shown in figure 3.1 a). Another mark on the other side of the crater is also needed to find the right orientation of the sample for the scan.

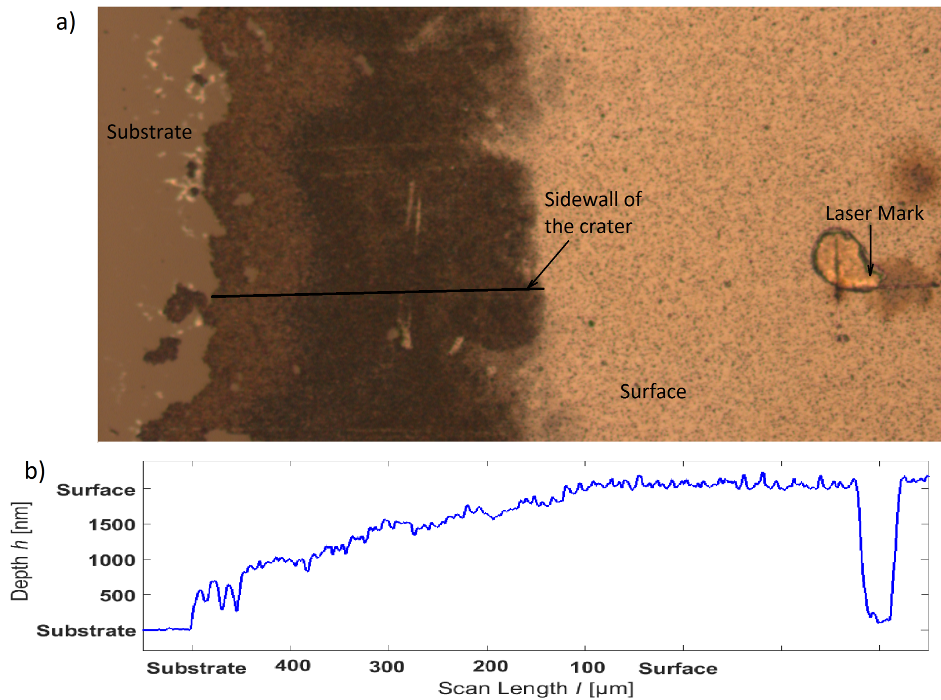

FIGURE 3.1: a) Microscopic image of the edge of a crater: The crater is etched by KOH, then the edge is marked with a laser mark to find the position again in Raman microscope, b) Depth profile of the sidewall scanned by Dektak profilometer: From right to left, the profile moves from the surface to substrate. The hole on the right side is the laser mark at the edge of the carter as in a).

3.2.4 Measuring Raman Spectra

The single monochromatic Raman setup is used in this case (discussed in chapter 2). After mounting the sample on the microscopic stage and finding the laser marks that give the right orientation of the desired sidewall for the scan by a 20x objective lens, a blue laser beam with a wavelength of 488 nm, a power of 540 µW, a width of 1 µm, and a length of 200 µm is focused on the first laser mark by a 50x objective lens.

After measuring the length of the sidewall, the start and end points have been selected so the scan starts before the edge of the crater and ends when reaching the glass. The number of points and spacing between them depend on the scan length. For the un-annealed and annealed amorphous silicon samples with a thickness of around 4.50 µm, 120 points with a spacing of 0.01 mm have been used. For the micro-crystalline sample with a thickness of 2 µm, 100 points with a spacing of 0.005 mm have been used. The 0.50 µm annealed sample needed only 40 points with a spacing of 0.0025 mm.

Two measurements have been done for each point to produce two spectra. The central grating positions are chosen at 509 nm and 535 nm; where the first spectrum shows the characteristics of vibrational phonon modes for Si-Si bonds in the region between 86 cm^{-1} and 1519 cm^{-1}, while the second spectrum shows the characteristics of vibrational phonon modes for Si-H bonds in the region between 1129 cm^{-1} and 2396 cm^{-1}. These two spectra overlap in the region between 1129 cm^{-1} and 1519 cm^{-1}, as shown in figure 3.2. During the analysis, the two spectra have been combined to produce one spectrum that covers the full region of interest from 86 cm^{-1} to 2396 cm^{-1}.

When the scan started, the laser source is fixed while the stage is moving automatically in y-direction for the 120 points with the selected spacing. There is also a gradient in the surface of the sample in the z-direction owing to the sidewall created during KOH etching. The stationary laser source is not in focus with depth during the measurement. This issue has been corrected during the analysis by normalization. Each spectrum of the 240 spectra has been measured for three accumulations to remove the spikes, each with an integration time of 60 seconds to reduce noise in the raw data. The setup has been automatically saving the data individually during the scan as ASCII files, which have been analyzed and matched with the depth profile coming from the Dektak profilometer later.

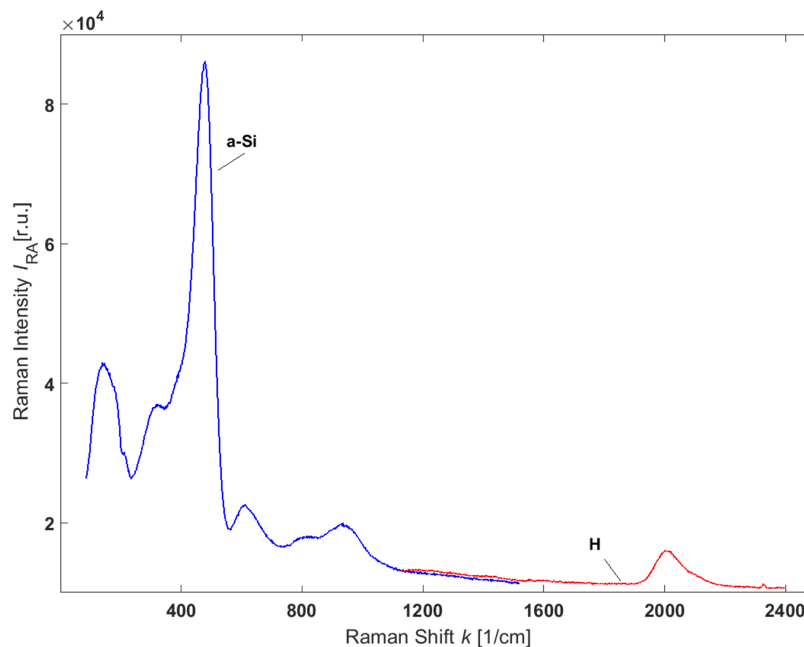

FIGURE 3.2: Raw data produced from a single monochromatic Raman setup. Two Raman spectra with overlapped region to combine them afterwards.

3.3 Raman Measurement for 2D Mapping

3.3.1 Samples Preparation

In this part, a nano-crystalline silicon sample has been deposited on glass by electron beam deposition (more details about EBD in [27]), with a thickness of 15 µm and size of 5x5 cm^2. A 500 nm SiO_2 layer has been deposited on top afterwards as a capping layer to prevent dewetting of the thin film during the crystallization process [11].

Since the LPC laser beam is only 1.24 cm in length, the large sample has been divided into five rectangular areas with a size of 0.80x1.50 cm^2 for each, as shown in figure 3.3. The areas have been demarcated by a fimto-second laser of 1026 nm wavelength and 500 mW to separate the crystallized silicon region from the amorphous silicon region during LPC process, and prevent any effect from having a transition region between the two areas during the process. The thickness of the lines is 1 mm so they can be visible during LPC process, hence the start point of the laser beam can be seen clearly and focused on the sample, so the system is not damaged by the laser. Finally, the rectangles have been cut by a glass cutting machine to prevent any effect from each other during the process.

After that, all samples have been mounted inside a high vacuumed chamber simultaneously, and annealed by heating them from room temperature to a temperature of 510 ^{o}C for 30 minutes before crystallization. The LPC laser beam has a wavelength of 808 nm. Different crystallization parameters (e.g.: scan speed and power) have been used as shown table 3.2 since they are the control parameters for resulting poly-crystalline silicon layers on glass. Finally, the samples have been left in the chamber to cool down for one day before taking them out.

TABLE 3.2: Laser LPC Parameters Summary

Sample Number	Power P [W]	Scan Speed V [mm/s]
1	45	1
2	55	2
3	65	3
4	75	4
5	85	5

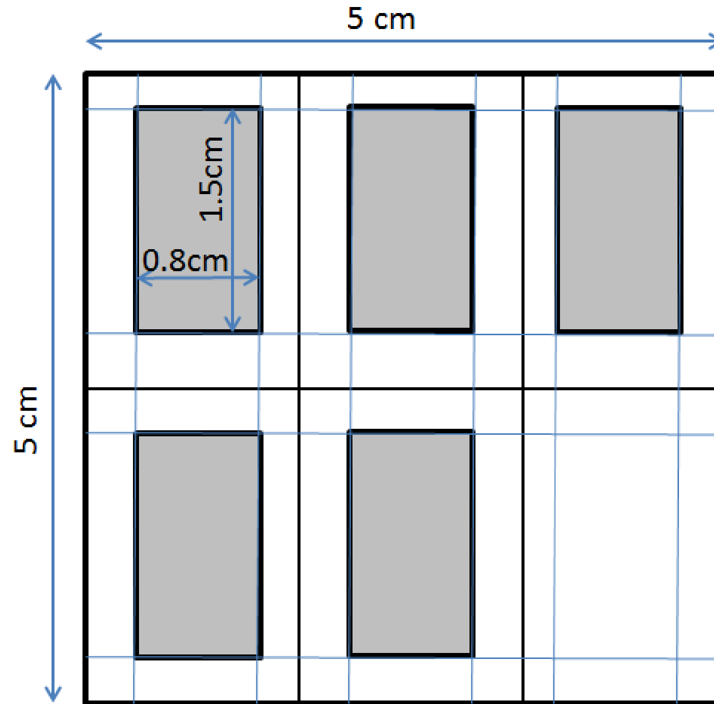

FIGURE 3.3: Schematic image of the sample layout. small rectangles with an area of 0.80x1.50 cm^2 for each have been demarcated by a fimto-second laser, then cut by a glass cutting machine.

3.3.2 Hydrofluoric Acid Etching

In order to remove the contribution from the capping layer and have a better focus control, wet dip chemical etching has been used to etch the 500 nm capping layer on top of LPC-Si layer. The etching process has been carried out with hydrofluoric acid (HF) with a concentration of 10 %. Dipping each sample in HF solution for 13 minutes has been enough to fully remove the 500 nm layer. The etching is done with the following reaction:

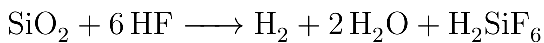

$$SiO_2 + 6\,HF \longrightarrow H_2 + 2\,H_2O + H_2SiF_6$$

3.3.3 Measuring Raman Spectra

The same blue laser source but with a circular spot of 1 µm diameter has been used in this case, with the double monochromatic Raman setup (discussed in chapter 2) to detect the c-Si peak region only. The measured Raman spectrum shows the characteristics of vibrational phonon modes of a c-Si structure in the range

between 219 $\mathrm{cm^{-1}}$ and 692 $\mathrm{cm^{-1}}$, in which TO mode is the only Raman active mode.

After the sample has been mounted on the microscopic stage, a manual scan has been done to search for stress as shifts in the c-Si peak away from 520 $\mathrm{cm^{-1}}$. After finding the position and while preparing for the scan; an optical light, an IR light, and the blue laser source have been focused on the sample for some time; this step heats up the sample and shifts c-Si peak away from its position. To prevent this issue, all light sources have been turned off for one hour to cool the sample down before turning on only the laser again and starting the scan immediately. This method has been applied to all measurements in this set of samples.

Since the blue laser has a penetration depth of 0.50 µm in case of c-Si structure, it is good to do the scan twice for each position. Once from surface side, while the other scan from glass side; to have the trend in stress with depth. In case of scanning from the surface side, an integration time of 5 seconds and two accumulations for each point have been used. While in case of scanning from the glass side, the intensity is lower because of glass; hence the integration time has been increased to 10 seconds for two accumulations to increase the intensity to have a better signal to noise ratio. During the scan, the laser spot is fixed while the stage is automatically moving in x- and y-directions with a dimension of 60x60 μm^2 and a spacing of 1 µm between points in both directions. Data has been saved manually in one sif. file at the end of the scan and converted to ASCII files later on.

Chapter 4

MATLAB for Data Analysis and Calculations

MATLAB software is a powerful and fast tool that uses a high level programming language for data analysis. Scripts as included in Appendix A are written by MATLAB software, that automatically imported ASCII files for the analysis. Each case needed a unique script that had to fit the type of the required data evaluation. Data correction, analysis, and calculations with MATLAB for the depth profiling as well as the two dimensional mapping are described in detail in this chapter.

4.1 Raman Measurement for Depth Profiling

4.1.1 Baseline Fitting

Figure 4.1 shows Raman spectrum in the region from $1129\,\mathrm{cm}^{-1}$ to $2396\,\mathrm{cm}^{-1}$, the baseline of this spectra is not leveled at zero because of noise effect. Hence a baseline fitting should be done to all spectra by using an external function from MATH Works as included in Appendix A, in which 10 points are selected along the baseline and away from the peaks regions. A curve is then generated between the points by 3rd order interpolation. Finally, the interpolated curve is subtracted from raw data, to make the baseline at zero level.

For the other spectrum in the region $1129\,\mathrm{cm}^{-1}$ and $1519\,\mathrm{cm}^{-1}$, the value of the last point on the spectrum is subtracted from raw data then combined to the first

spectrum to make them one that covers the full range of interest from 86 cm^{-1} to 2396 cm^{-1}, as shown in figure 4.2.

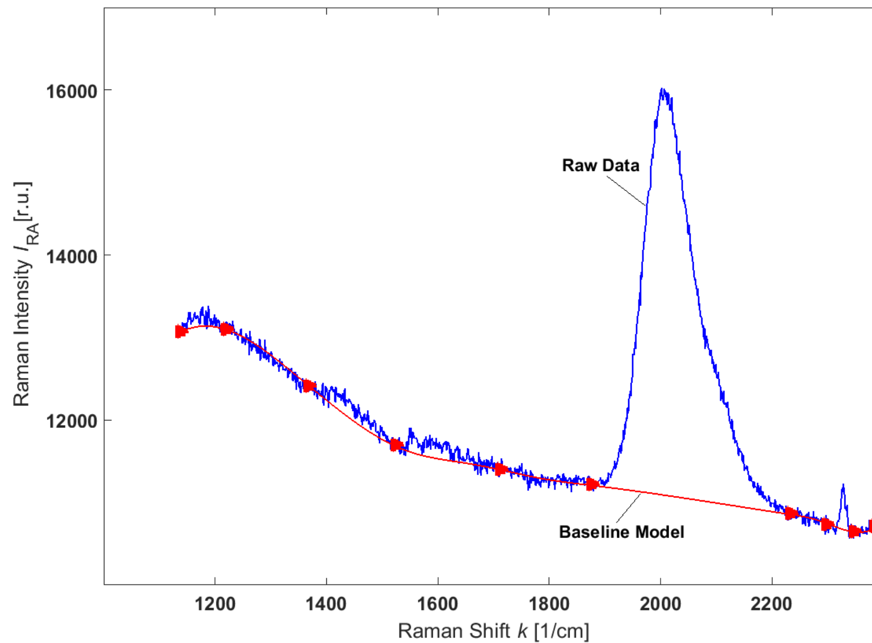

FIGURE 4.1: Baseline fitting for a Raman spectrum in the region between 1129 cm^{-1} and 1519 cm^{-1}, in which 10 points are selected on the base of the spectrum, then a curve is generated between them. Finally the curve is subtracted from raw data to make the baseline at zero level.

4.1.2 Normalization

As mentioned in the previous chapter, the laser is not in focus the whole time during the scan with depth; hence the spectra should be normalized according to the a-Si peak in the TO mode to remove this effect, since this peak does not change appreciably with depth. [17] Figure 4.2 shows the final corrected spectra after normalization.

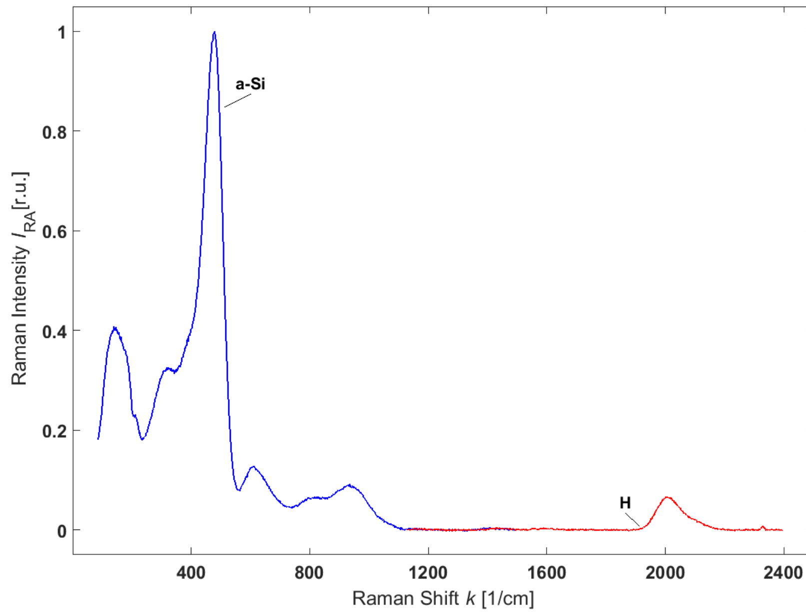

FIGURE 4.2: Final spectrum after normalization covers the full range of interest from 86 cm^{-1} to 2396 cm^{-1}. The two spectra are corrected, combined, and normalized with respect to a-Si peak.

4.1.3 Peaks Fitting and Calculations

An external function from MathWorks is used for peaks fitting [28]. The function used Bootstrap method to generate a model, estimate the standard deviation, make trails, and take the one with the lowest Root Mean Square Error fit. The model is generated according to peaks shapes, numbers, and positions. The integrated intensities under peaks are then used for the required evaluation.

Si-Si vibrational phonon modes in the region between 100 cm^{-1} and 600 cm^{-1} are needed to investigate whether PECVD deposited thin layer is micro-crystalline or amorphous silicon. In case of micro-crystalline materials, TA, LA, and LO are not active, while a complex TO peak is shifted close to 520 cm^{-1}, as discussed in chapter 2. Equation 2.6 is then used to quantify the degree of crystallinity within the structure.

In case of amorphous structure, the four vibrational modes are active. TO and TA peaks are the only modes needed for investigating MRO and SRO. Köhler [17] used the following method in his thesis, which has been adopted in this thesis as well. As shown in figure 4.3, TO mode is an asymmetrical peak, the left side is broader since it is combined to LO mode. To minimize this influence, only the

right side of the peak is taken from 480 cm^{-1} to 600 cm^{-1}, and fitted into one Gaussian peak. The integration under this part is then multiplied by two to give the total integrated intensity of TO mode, while the function gives FWHM as a total. To evaluate TA mode, the region between 100 cm^{-1} and 200 cm^{-1} is taken. A second baseline fitting is first needed to level the edge of the peak at zero and fitted into one Gaussian peak [17]. MRO and SRO are calculated afterwards according to equations 2.3 and 2.4, respectively.

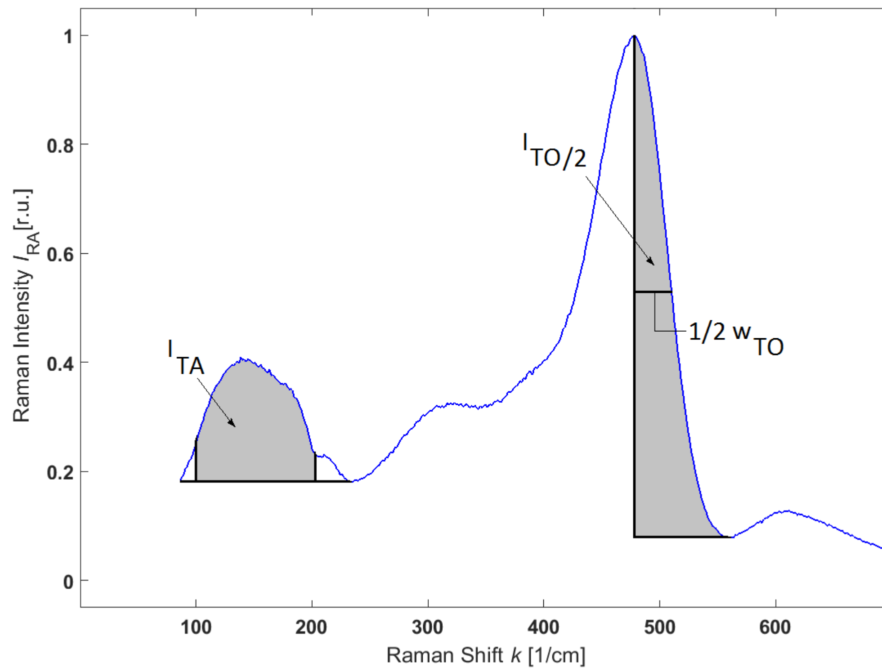

FIGURE 4.3: Rama spectrum for Si-Si vibrational phonon modes region in a-Si structure. Only the right side of TO mode is taken for calculation, while TA mode needs second baseline fitting before calculation.

For Si-H vibrational phonon modes, the region between 1990 cm^{-1} and 2200 cm^{-1} is needed to investigate hydrogen content and micro-structure parameters. The complex peak is fitted into two Gaussian peaks with fixed positions, as discussed in chapter 2. Equation 2.7 is then used to calculate micro-structure parameters.

4.2 Raman Measurement for 2D Mapping

4.2.1 Data Import

In this case, it is important to convert and separate raw data into individual files, and export them before any correction or evaluation. Baseline fitting is done in the same way as the previous section. While for normalization, c-Si peak is used.

4.2.2 Peaks Fitting and Calculations

TO mode is the only Raman active mode in case of crystalline silicon structures. Raman shift ranging between $510\,\mathrm{cm}^{-1}$ to $530\,\mathrm{cm}^{-1}$ is needed to investigate stress inside. The mode is fitted into one Lorentzian peak with a variable peak position, as discussed in chapter 2. Then, equation 2.5 is used to calculate the stress in MPa. The results are finally plotted in two dimensional maps.

4.2.3 Cracks Identification

In some scan areas where there is a crack, the light is not scattered and collected, instead only noisy signal is obtained. These points are found and identified by more filters in MATLAB scripts and set to a non value (NAN), so they are not included in the calculations afterwards.

Chapter 5

Results and Discussion

The main aim of the present thesis is to develop different Raman spectroscopy techniques as a helpful characterization method to investigate the properties of precursor layers deposited by PECVD and crystallized by LPC process, as depth profiling and 2D mapping. The results from the two different sets of samples that are scanned with Raman setups and analyzed with MATLAB software are presented and discussed in detail in this chapter.

5.1 Raman Measurement for Depth Profiling

The analysis and calculations as discussed in section 4.1 are done to all scanned points on the sidewall for each sample, then matched with the depth profile coming from the Dektak profilometer. These Raman measurements give more details about the changes in properties with depth.

5.1.1 Analysis of μc-Si:H

Figures 5.1 illustrates Raman spectra for vibrational phonon modes of the first sample at different depths, in a range between $100\,\text{cm}^{-1}$ and $600\,\text{cm}^{-1}$. Here, only one mode appears in the region between $400\,\text{cm}^{-1}$ and $600\,\text{cm}^{-1}$, which can be fitted into three Gaussian peaks, as described in section 2.4. Hence the sample has a micro-crystalline silicon structure. The relation between the three peaks gives the degree of crystallinity. Figure 5.2 illustrates the depth profile of crystallinity,

in which, the sample has a nearly constant crystallinity of 30 % for the first 600 nm near the surface, then it decreases gradually from 30 % to 10 % near the substrate.

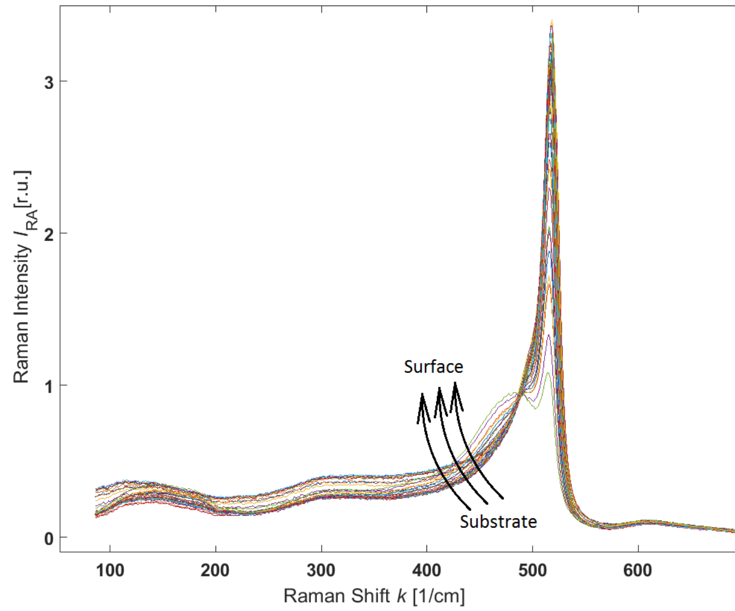

FIGURE 5.1: Raman spectra of the μc-Si sample. One mode appears in the region between 400 cm^{-1} and 600 cm^{-1}. 100 spectra for 100 points are measured and analyzed along the sidewall.

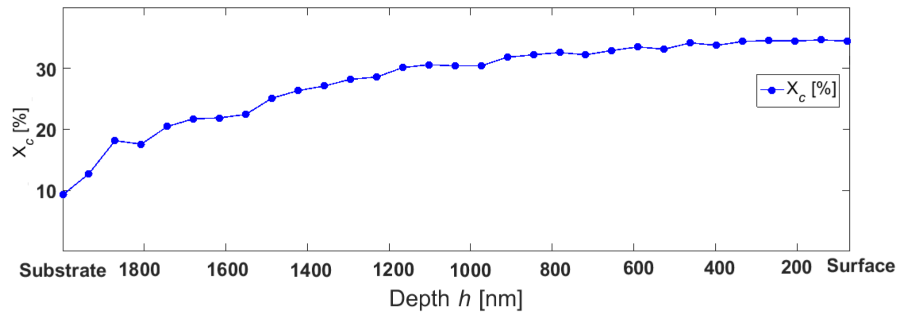

FIGURE 5.2: Depth profile of of crystallinity for μc-Si structure. Crystallinity is nearly constant near the surface and then decreases gradually from 30 % at the surface to 10 % near the substrate.

Figure 5.3 illustrates Raman spectra for vibrational phonon modes of Si-H bonds at different depths, the signal at 2330 cm^{-1} belongs to N_2 (air) detected during the measurements. In a range between 1900 cm^{-1} and 2200 cm^{-1}, Si-H peak appears at 2000 cm^{-1}, as well as Si-H_2 peak at 2100 cm^{-1}. The relation between the two peaks gives the micro-structure parameters as in figure 5.4, which illustrates the depth profile of hydrogen content and micro-structure parameters. Hydrogen content is

nearly constant with depth except for a few points near the surface. Hence microstructure parameters has the same behavior as well, only few points seem to be different.

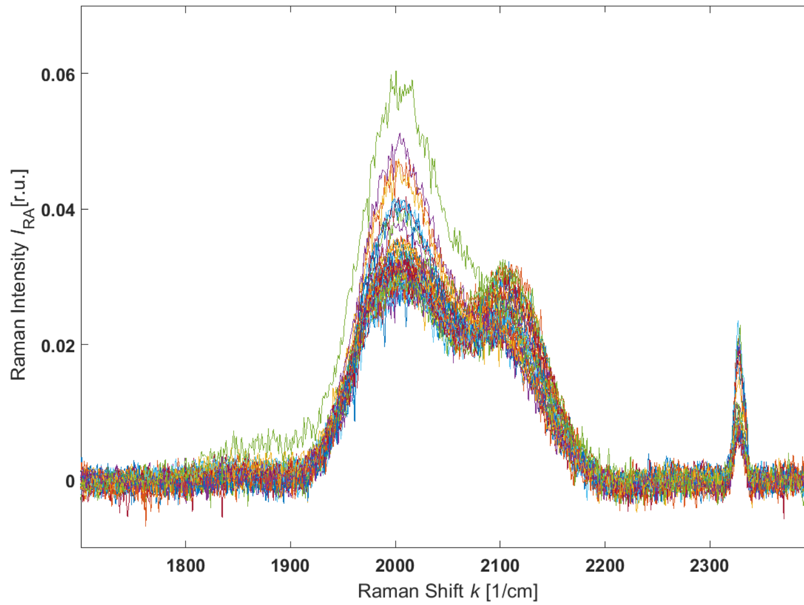

FIGURE 5.3: Raman spectra of Si-H vibrational phonon modes for µc-Si structure. 100 spectra for 100 points are measured and analyzed along the sidewall.

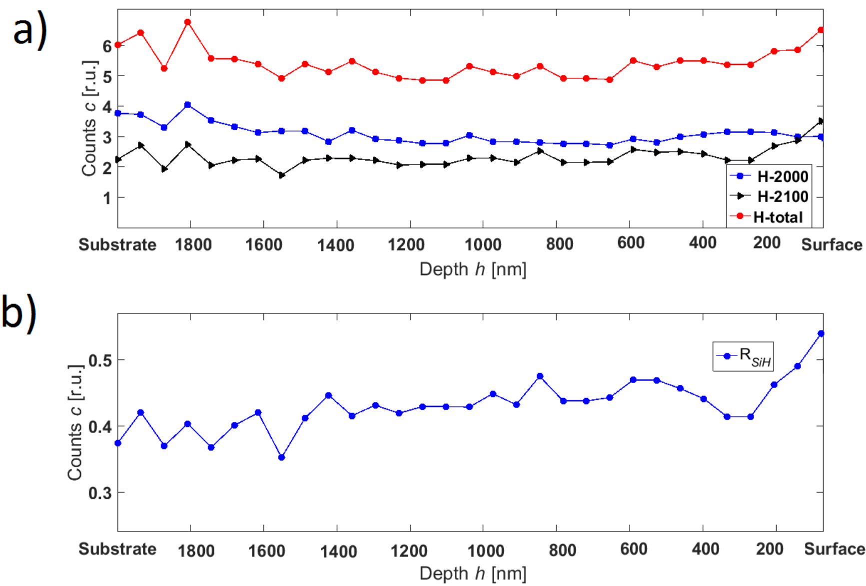

FIGURE 5.4: Depth profile of a) hydrogen content b) microstructure parameters. Both are nearly constant with depth.

5.1.2 Analysis of a-Si:H Before Annealing

The other two samples show different thermal behaviour after annealing. The first sample is thermally unstable; only 0.50 µm of the material remains on glass. This sample is called "unstable sample" in the following discussions. The other sample is thermally stable, the whole thickness remains unchanged during annealing. This sample is called "stable sample". Therefore a comparison between their properties before annealing is needed.

Figure 5.5 illustrates Raman spectra of the other two samples before annealing at different depths, in the range between $100\,\mathrm{cm}^{-1}$ and $600\,\mathrm{cm}^{-1}$. In these spectra, TO, LO, LA, TA modes appear at $480\,\mathrm{cm}^{-1}$, $390\,\mathrm{cm}^{-1}$, $314\,\mathrm{cm}^{-1}$, and $140\,\mathrm{cm}^{-1}$ respectively. Hence both samples have an amorphous silicon structure. The ratio between the TO and TA modes gives MRO, while the width of TO mode gives SRO; as presented in chapter 2. Note that for the stable sample, a very small c-Si peak at $520\,\mathrm{cm}^{-1}$ appears in the spectra. The c-Si peak means that the sample is at the edge of µc-Si structure, but it is very small and can not be used to determine the crystallinity of the sample; hence the sample has an a-Si:H structure.

Figure 5.6 illustrates the depth profiles of structural order in the medium and short ranges for both stable and unstable samples. For the unstable sample (the grey colored depth profiles), MRO decreases gradually from 6 r.u. at the surface to 4 r.u. at mid-depth, then it is nearly constant for the remaining thickness. SRO is nearly constant with depth. While for the stable sample (the blue colored depth profiles), MRO is nearly constant for the whole thickness. SRO is also constant with depth, but with higher quantity than the unstable sample.

Figure 5.7 illustrates Raman spectra of Si-H bonds of both samples. Figure 5.8 and 5.9 show depth profiles of hydrogen content and micro-structure parameters for both. Hydrogen content and micro-structure parameters are nearly constant for both samples but with higher quantity for the unstable one.

The two amorphous samples show different structural order properties before annealing, but it is still not yet clear if these are the control parameters for the thermal behaviour of samples after annealing. More investigation has been done for both samples after the annealing process in the following section.

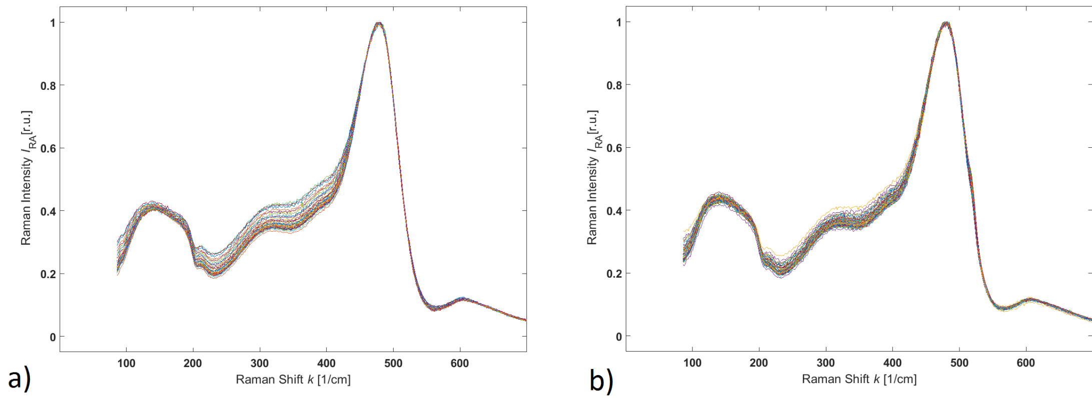

FIGURE 5.5: a) Raman spectra of the unstable a-Si sample before annealing b) Raman spectra of the stable a-Si sample before annealing. 120 spectra for 120 points are measured and analyzed along the sidewall of both samples. The four vibrational modes are Raman active.

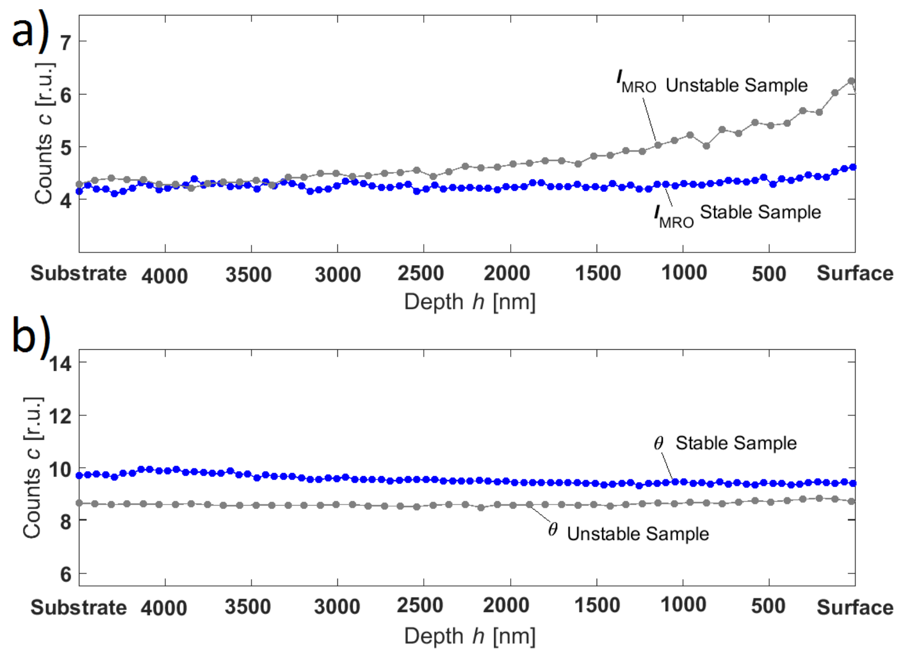

FIGURE 5.6: Depth profile of a) Medium range order b) Short range order for the a-Si samples before annealing. The grey colored depth profiles belong to the unstable sample for the mean of the comparison. The blue colored depth profiles belong to the stable sample. For the unstable sample, MRO decreases for the 1st half of the thickness then becomes constant for the 2nd half, while it is nearly constant for the whole thickness for the stable sample. SRO is nearly constant for both samples but with higher quantity for the stable sample.

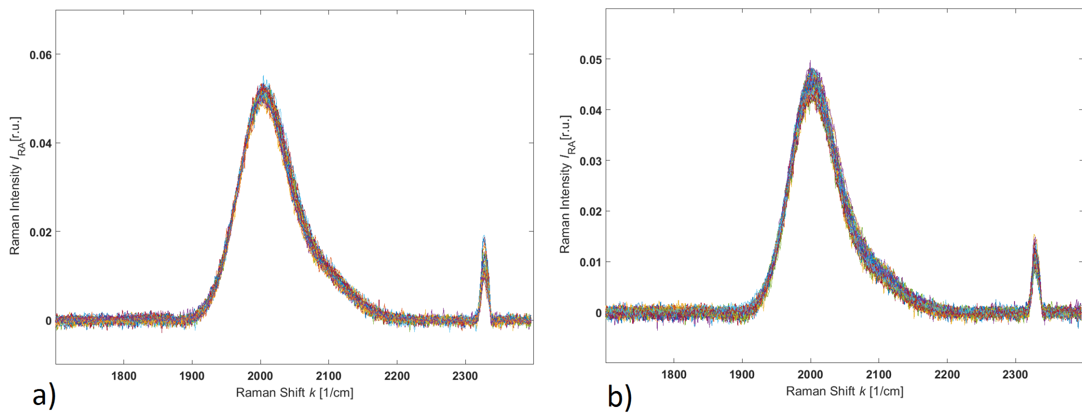

FIGURE 5.7: a) Raman spectra of Si-H bonds of the unstable a-Si sample before annealing b) Raman spectra of Si-H bonds of the stable a-Si sample before annealing. 120 spectra for 120 points are measured and analyzed along the sidewall for both samples.

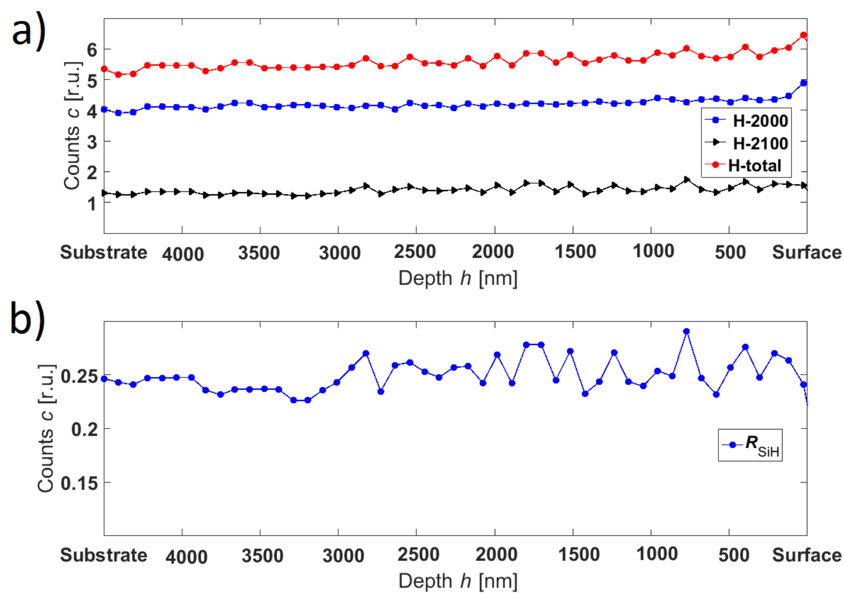

FIGURE 5.8: Depth profile of a) Hydrogen content b) Micro-structure parameters for the unstable sample before annealing. Both hydrogen content and micro-structure parameters are constant with depth, only few points seem to have different behavior.

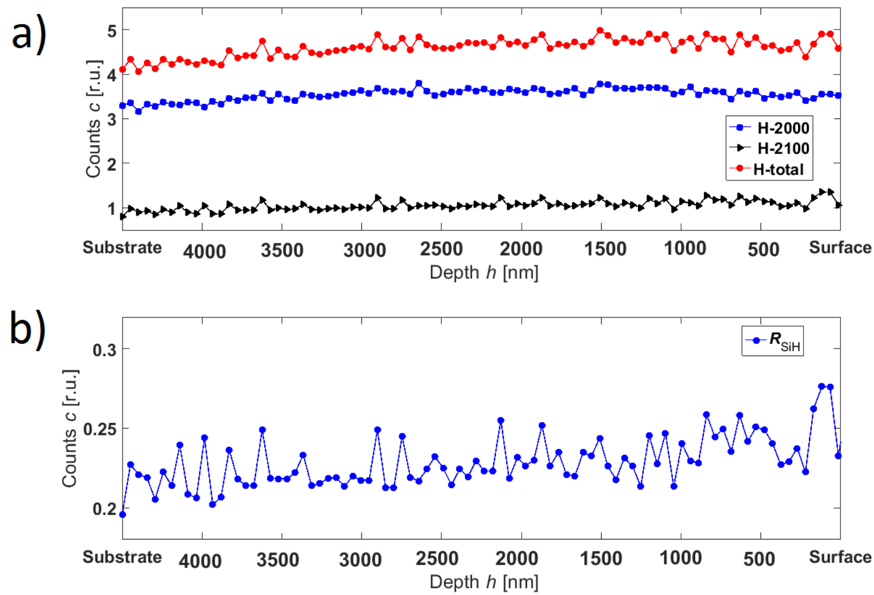

FIGURE 5.9: Depth profile of a) Hydrogen content b) Micro-structure parameters for the stable sample before annealing. Both hydrogen content and micro-structure parameters are constant with depth, only few points seem to have different behavior.

5.1.3 Analysis of a-Si:H After Annealing

After annealing the two amorphous samples, a comparison has been done for each sample before and after annealing to investigate the influence of annealing on the structural order and hydrogen diffusion. For the unstable sample, since only 0.50 µm remains after annealing, the properties of only the first 0.50 µm from the un-annealed sample is taken for the mean of the comparison. Figure 5.10 indicates that the four vibrational modes are still visible in the unstable sample after annealing; hence the sample still in the amorphous phase. Figure 5.11 illustrates the properties of the unstable sample before and after annealing, it is notable from the depth profiles that the behavior of both MRO and SRO after annealing changes after annealing. Before annealing, Both MRO and SRO are constant with depth. After annealing, MRO decreases gradually with depth. SRO is nearly constant for the first 400 nm but with much higher quantity than before, then decreases for the last 100 nm. Figures 5.12 and 5.13 indicate that almost all hydrogen diffuses and barely detected by Si-CCD camera; hence micro-structure parameters can not be calculated.

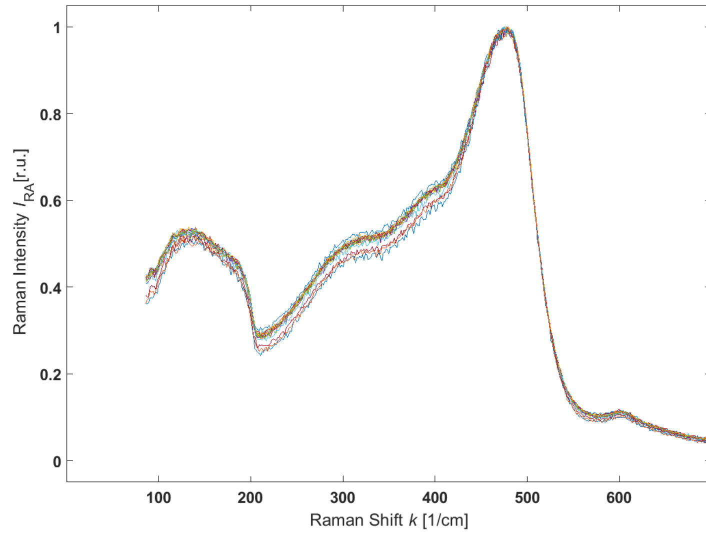

FIGURE 5.10: Raman spectra of vibrational phonon modes for the unstable sample after annealing. The four vibrational phonon modes are still Raman active; hence the sample has an a-Si structure. Only 40 spectra for 40 points are measured and analyzed along the sidewall.

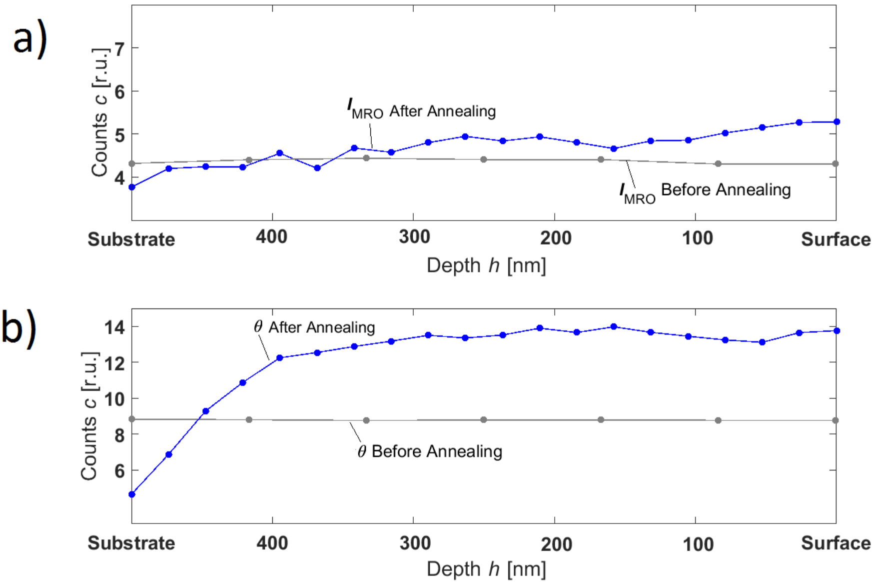

FIGURE 5.11: Depth profile of a) Medium range order b) Short range order for the unstable sample before and after annealing. The grey colored depth profiles belong to the properties before annealing.The blue colored depth profiles belong to the properties after annealing. Before annealing, Both MRO and SRO are constant with depth. After annealing, MRO decreases gradually with depth. SRO is nearly constant for the first 400 nm but with much higher quantity than before, then decreases for the last 100 nm.

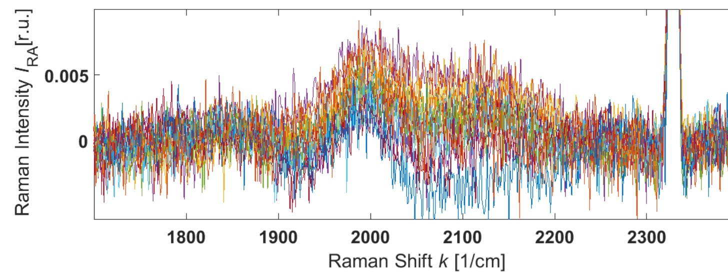

FIGURE 5.12: Raman Spectra for Si-H vibrational phonon modes for the unstable sample after annealing. almost all hydrogen diffuses and barely detected by Si-CCD camera. Only 40 spectra for 40 points are measured and analyzed along the sidewall.

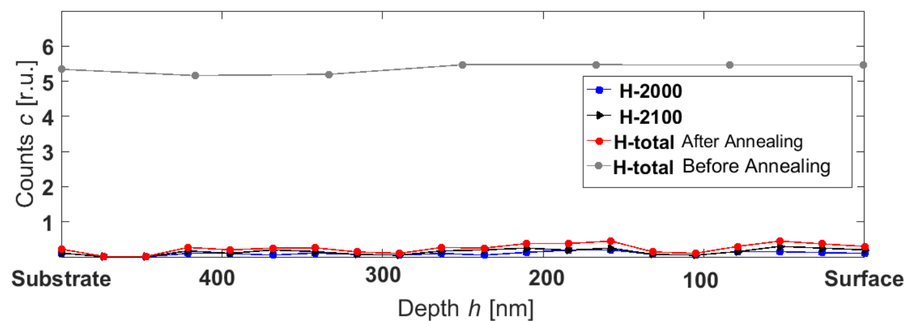

FIGURE 5.13: Depth profile of hydrogen content for the unstable after annealing. The grey colored depth profile belongs to hydrogen content of the same sample before annealing. Almost all hydrogen diffuses and barely detected by Si-CCD camera.

For the stable sample, the whole thickness remains unchanged during the annealing process; hence the whole depth profile of the un-annealed sample is taken for the comparison. As indicated in figure 5.14, a very small peak is visible at 520 cm^{-1}; therefore the sample comes to the edge of μc-Si structure with a crystallinity of 0.5 %. TA mode is still Raman active; hence it is still possible to calculate MRO and SRO as indicated in figure 5.15. MRO is still constant and has similar quantity as before annealing. SRO is still constant as well, but with slightly higher quantity than before annealing.

Figures 5.16 and 5.17 indicate that almost all hydrogen diffuses and barely detected with Si-CCD camera; hence micro-structure parameters can not be calculated. Note that for this sample, the precursor layer has many holes after annealing because of hydrogen diffusion. This has no influence on LPC process afterwards. But KOH etching is not successful to create a new crater without neither holes nor steeps; hence same crater has been taken before and after annealing.

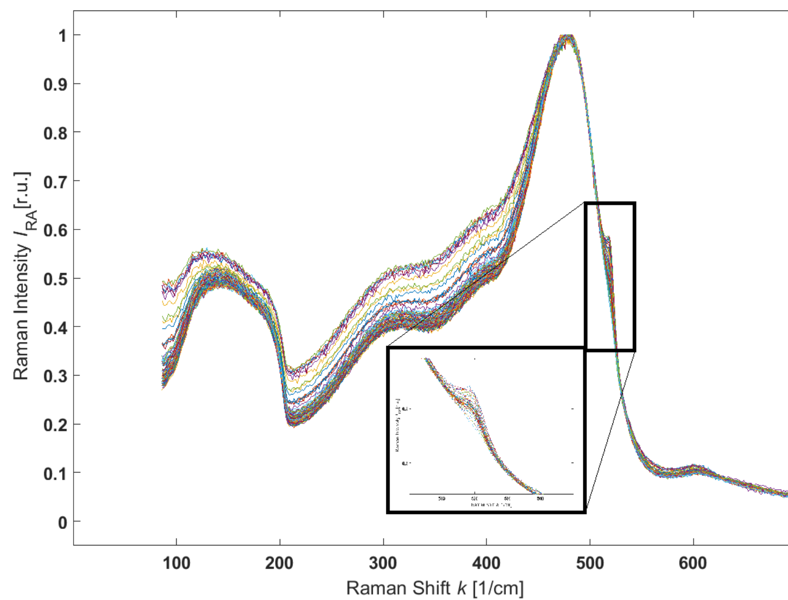

FIGURE 5.14: Raman spectra of vibrational phonon modes for the stable sample after annealing. The sample comes to the edge of a micro-crystalline structure with a crystallinity of 0.5 % only, TA mode is still Raman active; hence MRO and SRO can be calculated. 120 spectra for 120 points are measured and analyzed along the sidewall.

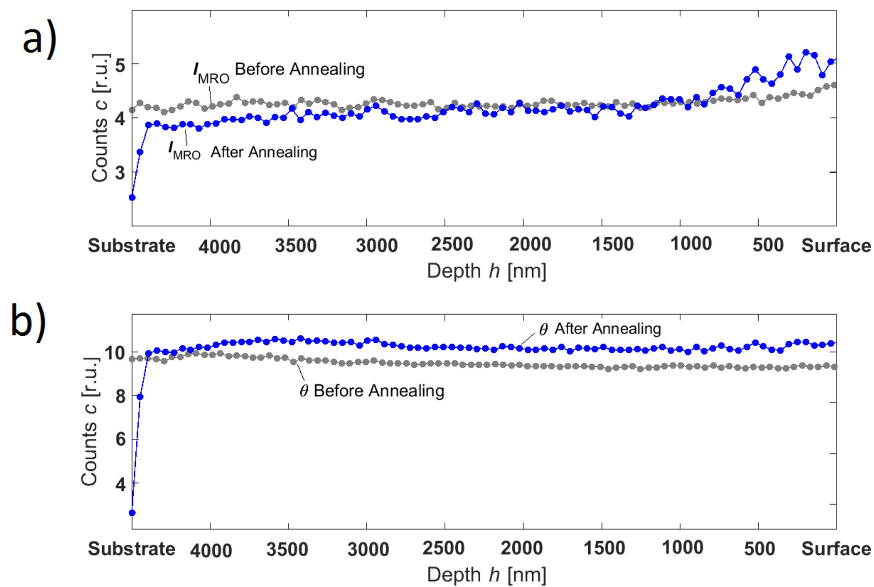

FIGURE 5.15: Depth profile of a) Medium range order b) Short range order for the stable sample before and after annealing. The grey colored depth profiles belong to the properties before annealing. The blue colored depth profiles belong to the properties after annealing. MRO is still constant and has similar quantity as before annealing. SRO is still constant as well, but with slightly higher quantity than before annealing.

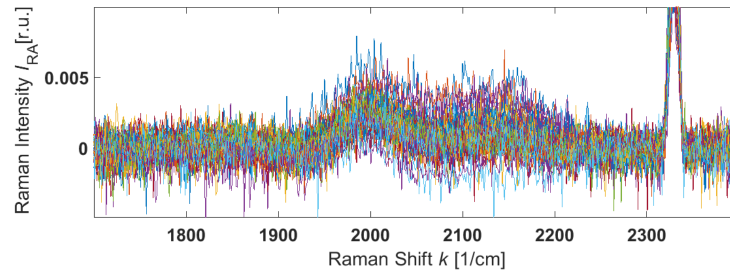

FIGURE 5.16: Raman spectra for Si-H vibrational phonon modes for the stable sample after annealing. Almost all hydrogen diffuses and barely detected by Si-CCD camera. 120 spectra for 120 points are measured and analyzed along the sidewall.

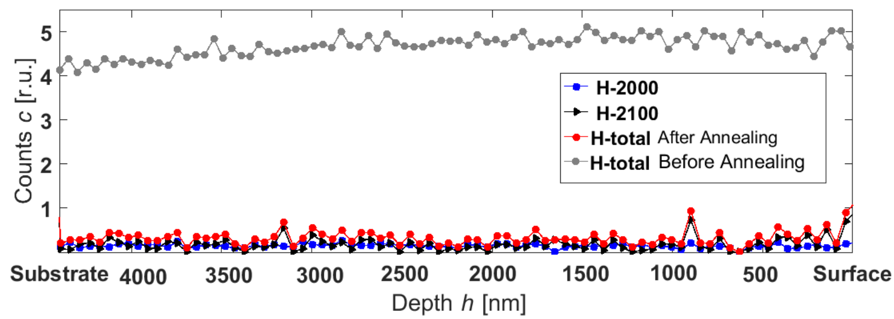

FIGURE 5.17: Depth profile of hydrogen content for the stable sample after annealing. The grey colored depth profile belongs to hydrogen content of the same sample before annealing. Almost all hydrogen diffuses and barely detected by Si-CCD camera.

In summary, there is a remarkable difference in the structural order between the two amorphous samples after annealing. The unstable sample illustrates changes in the behavior of MRO and SRO after annealing. Bfore annealing, MRO and SRO are nearly constant with depth. After annealing, MRO decreases gradually with depth, while SRO is nearly constant but has a much higher quantity than before annealing for the first 300 nm and then decreases gradually for the last 100 nm. The stable sample illustrates similar behavior of MRO and SRO after annealing. MRO and SRO have constant depth profiles before and after annealing. However, it is still not yet clear if these properties are the control parameters for the thermal behavior and stability of samples. More investigations should be done in the future, to prove that this trend is noticed on other samples as well.

5.2 Raman Measurement for 2D Mapping

After crystallization and with the help of a microscope, all samples have been found to be fully crystallized with the selected parameters. The difference between them is the type and density of defects that are presented on glass side as well as in the material itself. Defects in the precursor layer itself are a reflection of a residual stress between atoms which could be due to a grain boundary between two grains, a crack as a relaxation in high tensile stressed areas, or a buckling as a relaxation in high compressive stressed areas. [18]

The first sample, crystallized with a scan speed of 1 mm/s and power of 45 W is deformed. The capping layer has been molten into the first micrometer of the LPC-Si layer, with no cracks neither in glass nor in the material. The second sample, crystallized with scan speed of 2 mm/s and power of 55 W has two cracks only in the material and no cracks on the glass side. The last three samples crystallized with scan speeds of 3, 4, and 5 mm/s and powers of 65, 75, and 85 W, respectively, have cracks in the glass side as well as in the material itself. The residual stress in the LPC-Si precursor layers are investigated by Raman spectroscopy.

In all presented 2D maps, c-Si peak position is found in a range between 518 cm^{-1} and 521 cm^{-1}, which ranged between a tensile stress up to 500 MPa and a compressive stress up to 300 MPa, as bi-axial stress. Two color bars are set for each map on the right side of each image, the first bar is set for Raman shift in wavenumbers, while the second is for stress in MPa. The yellow color is the reflection of a stress free at c-Si peak position of 520 cm^{-1}. The blue color is a reflection of tensile stress at lower wavenumbers. While the red color is a reflection of compressive stress at higher wavenumbers. While in microscopic images, bubbles are crystalline silicon structure formed during the crystallization process. While straight lines indicate grain boundaries within the structure. Each 2D map is matched with its microscopic image from the camera.

5.2.1 Non Stressed Areas

Areas away from any form of defects have been scanned by Raman spectroscopy to investigate the stress inside them. Figure 5.18 illustrates a scanned area of 60x60 μm^2. c-Si peak is in a range between 519.8 cm^{-1} and 520 cm^{-1}; hence a very

low stress variation is found in these positions ranging between a tensile stress up to 50 MPa and a compressive stress up to 75 MPa only.

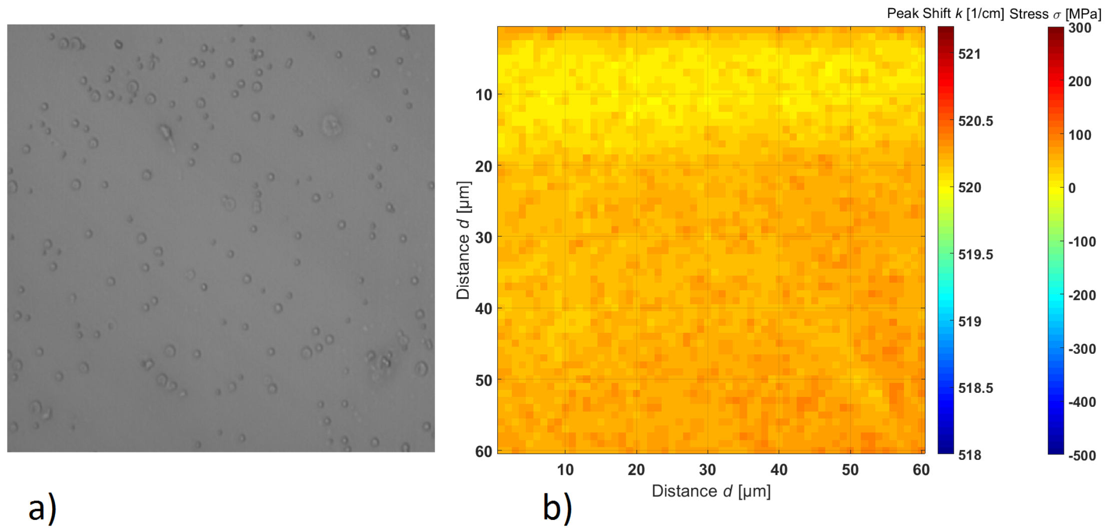

FIGURE 5.18: a) Microscopic image b) 2D map of Raman shift and stress for a stress free area. In the microscopic image, bubbles are c-Si structure formed during crystallization. In the 2D map,c-Si peak is in a range between 519.8 cm^{-1} and 520 cm^{-1}; hence a very low stress variation is mapped, ranging between a tensile stress behavior up to 50 MPa and a compressive stress behavior up to 75 MPa only.

5.2.2 Grain Boundaries Areas

A grain boundary forms when two grains with different orientations meet [29]. Figures 5.19 and 5.20 show boundaries between two different grains. These boundaries are visible as straight lines in the microscopic images which are correlated to a c-Si peak position shifting away from 520 cm^{-1} in a range between 520 cm^{-1} and 518.5 cm^{-1} in the 2D maps. Hence tensile stressed behaviour with a value up to 400 MPa is mapped as blue lines.

To investigate the changes in stress with depth around these defects, a grain boundary has been measured and mapped twice, once from the surface side while the other from the silicon-glass interface, as indicated in figures 5.21 and 5.22. From the surface side, c-Si peak position is shifting towards wavenumbers in a range between 520 cm^{-1} and 519.5 cm^{-1}. From the glass side, the peak is shifting towards lower wavenumbers in a range between 520 cm^{-1} and 518 cm^{-1}. Hence tensile stress increases with depth from 100 MPa at the surface to a value up to 400 MPa at the silicon-glass interface.

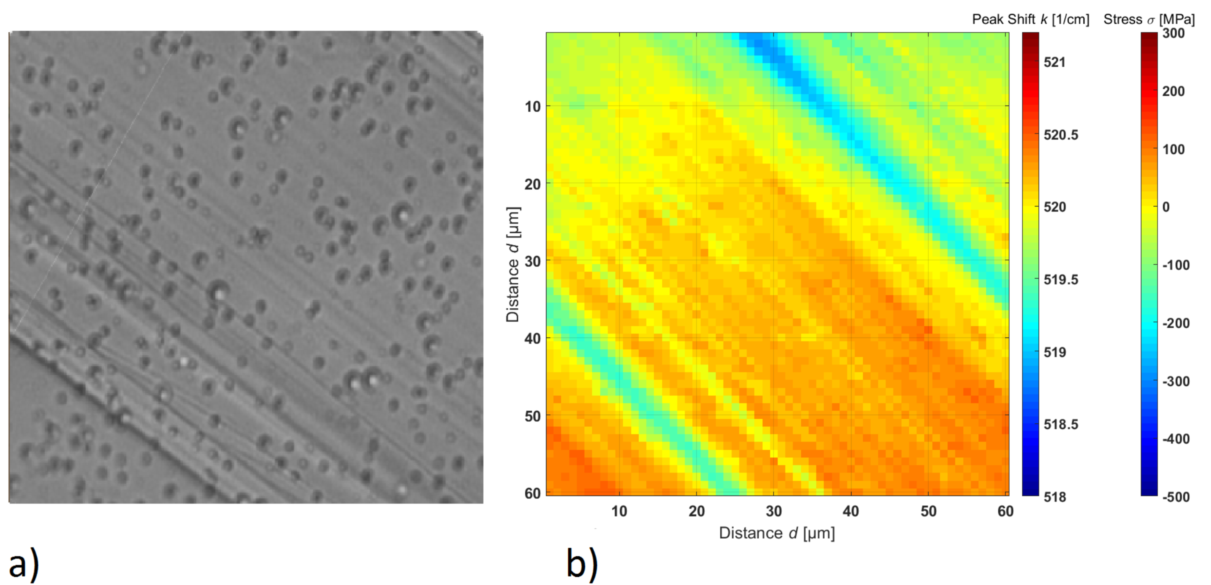

FIGURE 5.19: a) Microscopic image b) 2D map of Raman shift and stress for a grain boundary. In the microscopic image, bubbles are c-Si formed during crystallization, while the lines indicate grain boundaries and other defects in the sample. In the 2D map, c-Si peak is shifting towards lower wavenumbers; hence a tensile stress behavior up to 400 MPa is mapped as blue lines.

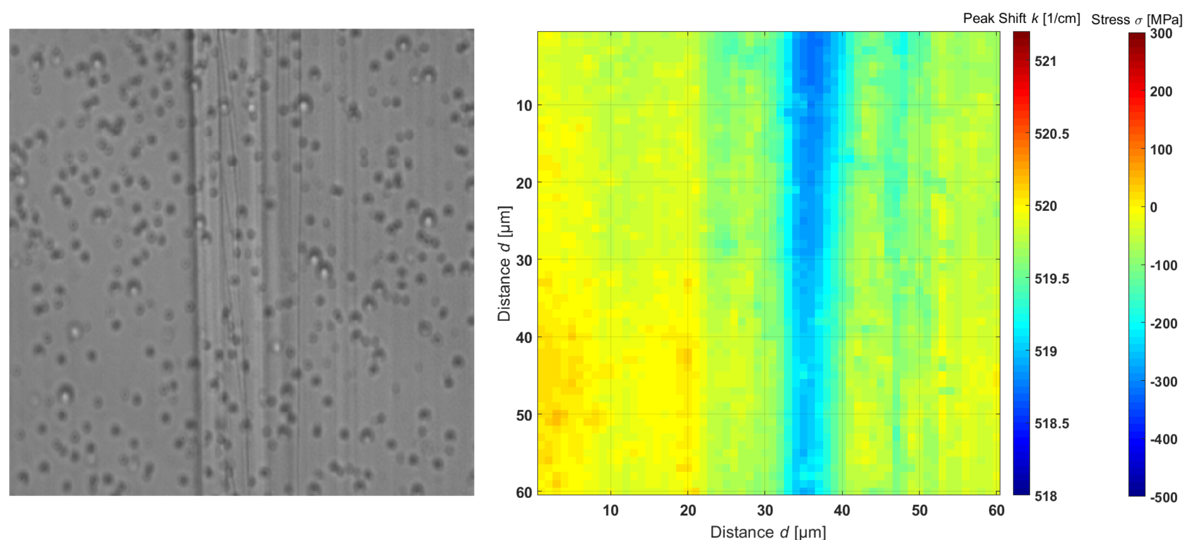

FIGURE 5.20: a) Microscopic image b) 2D map of Raman shift and stress for a grain boundary. In the microscopic image, bubbles are c-Si formed during crystallization, while the lines indicate grain boundaries and other defects in the sample. In the 2D map, c-Si peak is shifting towards lower wavenumbers; hence a tensile stress behavior up to 400 MPa is mapped as blue lines.

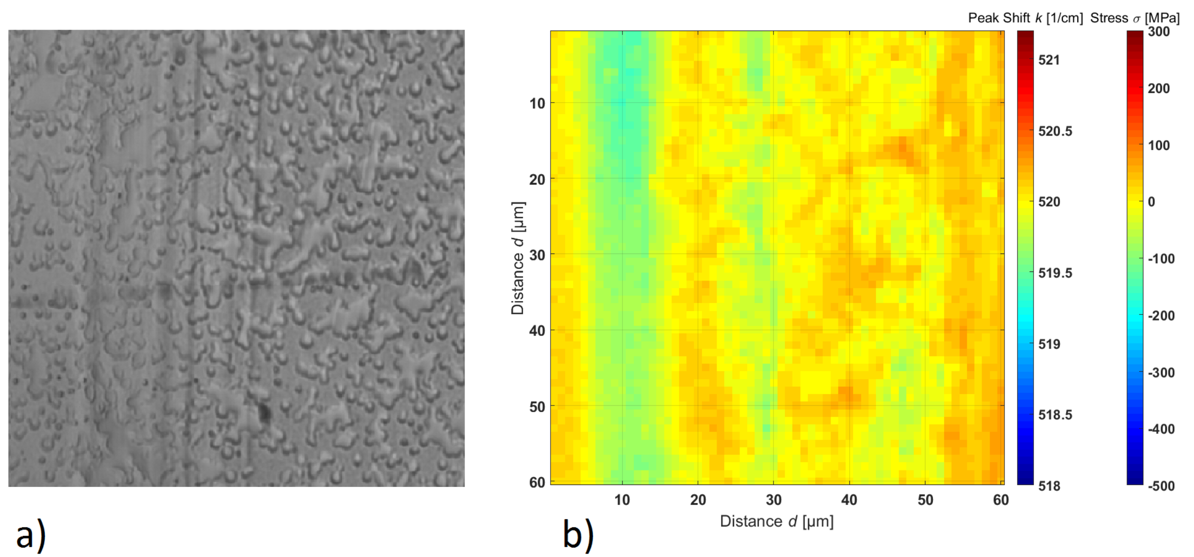

FIGURE 5.21: a) Microscopic image b) 2D map of Raman shift and stress for a grain boundary from surface side. In the microscopic image, bubbles are c-Si formed during crystallization, while the lines indicate grain boundaries and other defects in the sample. In the 2D map, c-Si peak is shifting toward lower wavenumbers in a range between $520\,\mathrm{cm}^{-1}$ and $519.5\,\mathrm{cm}^{-1}$; hence tensile stress up to 100 MPa is mapped as light blue lines.

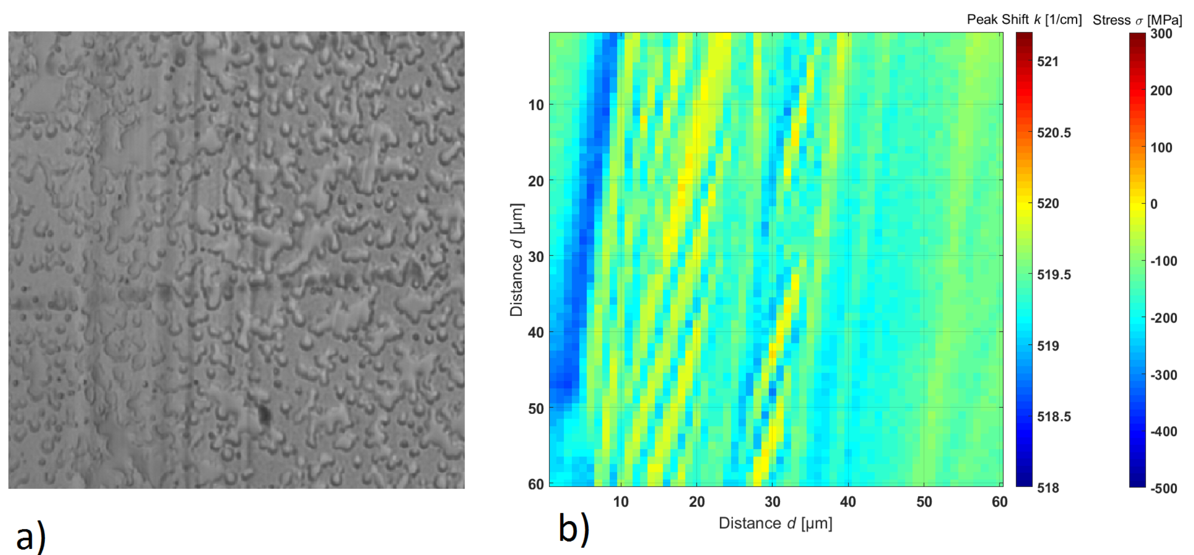

FIGURE 5.22: a) Microscopic image b) 2D map of Raman shift and stress for a grain boundary from glass side. In the microscopic image, bubbles are c-Si formed during crystallization, while the lines indicate grain boundaries and other defects in the sample. In the 2D map, c-Si peak is shifting more toward lower wavenumbers in a range between $520\,\mathrm{cm}^{-1}$ and $518\,\mathrm{cm}^{-1}$; hence higher tensile stress up to 400 MPa is mapped as dark blue lines.

5.2.3 Cracked Areas

When tensile stress is high enough, it relaxes plastically in a form of a crack. The crack occurs along the grain boundary giving a complex stress distribution, which varies between compressive on one side of the crack and tensile stresses on the other side. All cracked samples have cracks with the same shape but with different number. Higher scan speeds and power during LPC process lead to higher number of cracks in the sample. Different positions along a crack (middle of the crack as well as the crack tip) are investigated with Raman spectroscopy as indicated in figure 5.23. To investigate the changes in stress with depth around these cracks, some positions are scanned twice, once form the surface side and the other from the silicon-glass interface.

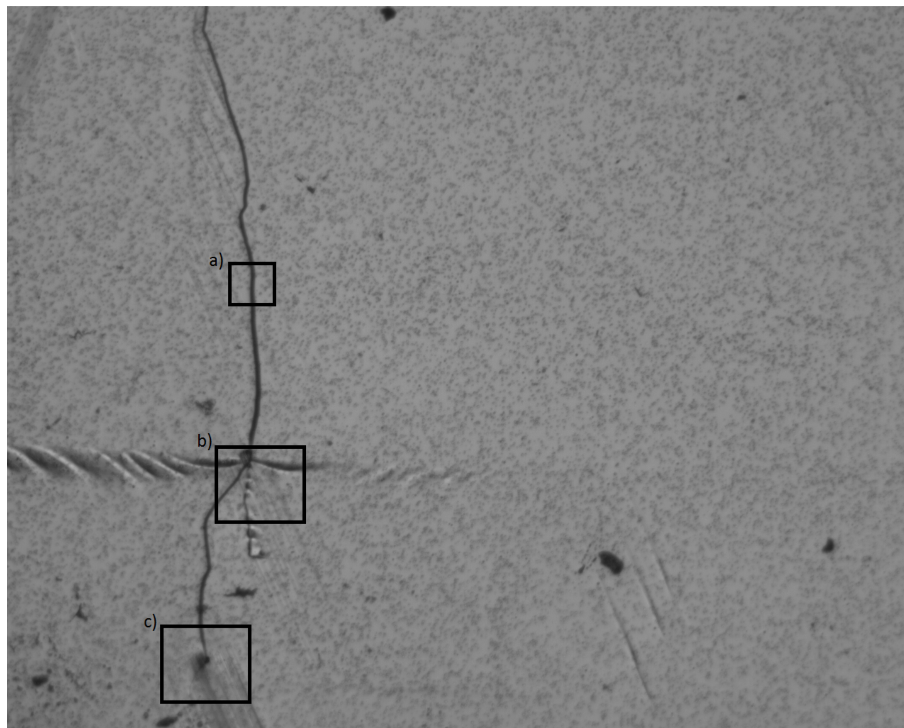

FIGURE 5.23: Microscopic image for the selected areas for Raman measurement, in a) and b) middle of a crack c) crack tip

Figure 5.24 illustrates a scanned area of 30x30 μm^2, in which the c-Si peak position is ranging between lower wavenumbers up to 518 cm^{-1} on the right side of the crack and higher wavenumbers up to 521 cm^{-1} on the left side. Hence the stress behavior is different between the two sides of the crack, ranging between a tensile stress behavior up to 500 MPa on the right side and a compressive stress behavior up to 250 MPa on the left side. The crack itself is mapped as a NAN value in the 2D maps.

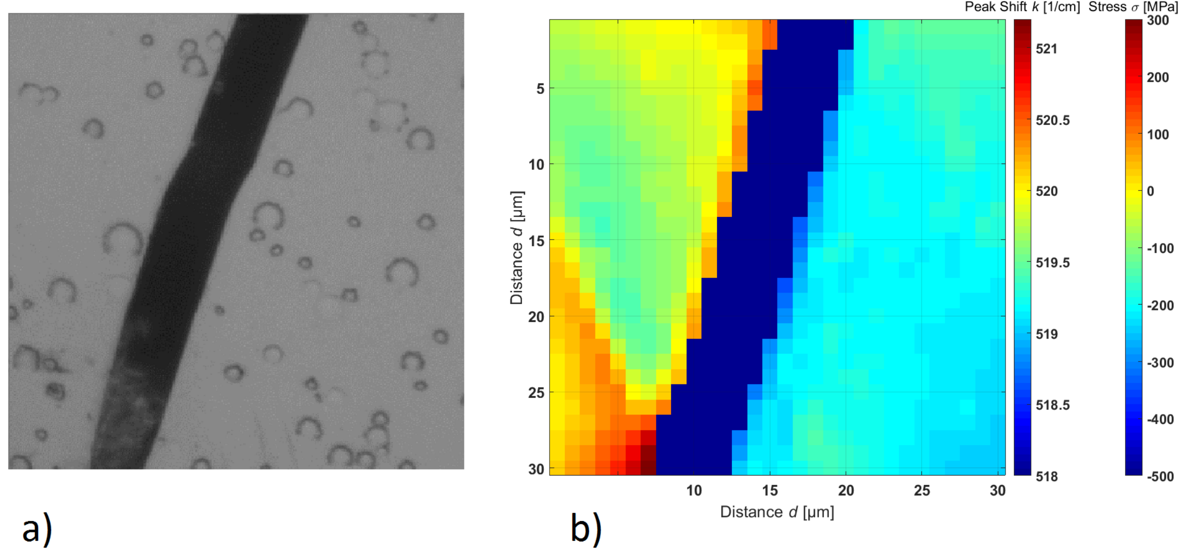

FIGURE 5.24: a) Microscopic image of the crack b) 2D map of Raman shift and stress for a cracked area. In the microscopic image, bubbles are c-Si formed during crystallization, while the black area indicates the crack in the sample. In the 2D map, c-Si peak is ranging between 518 cm^{-1} on the right side and 521 cm^{-1} on the left side of the crack. Hence the stress behavior is different on the two sides of the crack, ranging between a tensile stress behavior up to 500 MPa on the right side and a compressive stress behavior up to 250 MPa on the left side of the crack.

To investigate the changes in stress with depth, figures 5.25 and 5.26 show an area of 60x60 μm^2 scanned twice; once from surface side while the other from glass side. The first map from surface side illustrates a range of c-Si peak position between 519.8 cm^{-1} and 518 cm^{-1}. A tensile stress behavior is resulted on the two sides of the crack with a value up to 500 MPa. Going with depth, the second map from glass side illustrates a wider range of c-Si peak position between 520.5 cm^{-1} and 518.5 cm^{-1}. A tensile stress behavior up to 400 MPa is resulted on the right side of the crack. While a compressive stress behavior up to 125 MPa is resulted on the left side.

Figures 5.27 and 5.28 show the crack tip scanned twice in an area of 60x60 μm^2. The first map from surface side illustrates a range of c-Si peak position between 520.8 cm^{-1} and 519 cm^{-1}. Hence a stress behavior varying between a tensile stress up to 250 MPa and a compressive stress up to 200 MPa is mapped in the same position. The crack does not continue with depth as indicated in the second map; but higher tensile stress is noticed around the scanned area from the glass side with c-Si peak position up to 519 cm^{-1} and tensile stress behavior up to 250 MPa. Apparently this value is lower than the threshold to form a crack. Note that the

threshold value has not been detected since the crack releases the stress inside the structure.

In summary, the stress inside c-Si precursor layers crystallized by laser LPC process can be detected by Raman spectroscopy as a shift in c-Si peak away from 520 cm^{-1}. Lower wavenumbers indicates a tensile stress behavior while higher wavenumbers indicate a compressive stress behavior. In case of grain boundaries, tensile stress behavior is mainly detected and mapped. In case of cracks, stress behavior is varied between tensile stress on one side of the crack and compressive stress on the other side.

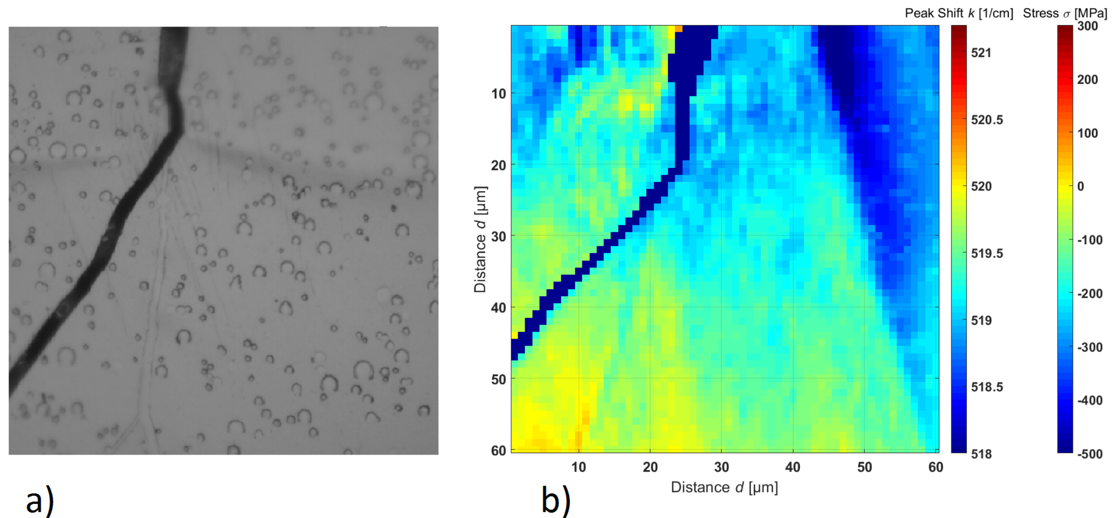

FIGURE 5.25: a) Microscopic image b) 2D map of Raman shift and stress for a cracked area from the surface side. In microscopic image, bubbles are c-Si formed during crystallization while the black area indicates the crack. In 2D map, c-Si peak is ranging between 519.8 cm^{-1} and 518 cm^{-1}. A tensile stress behavior up to 500 MPa is mapped on both sides.

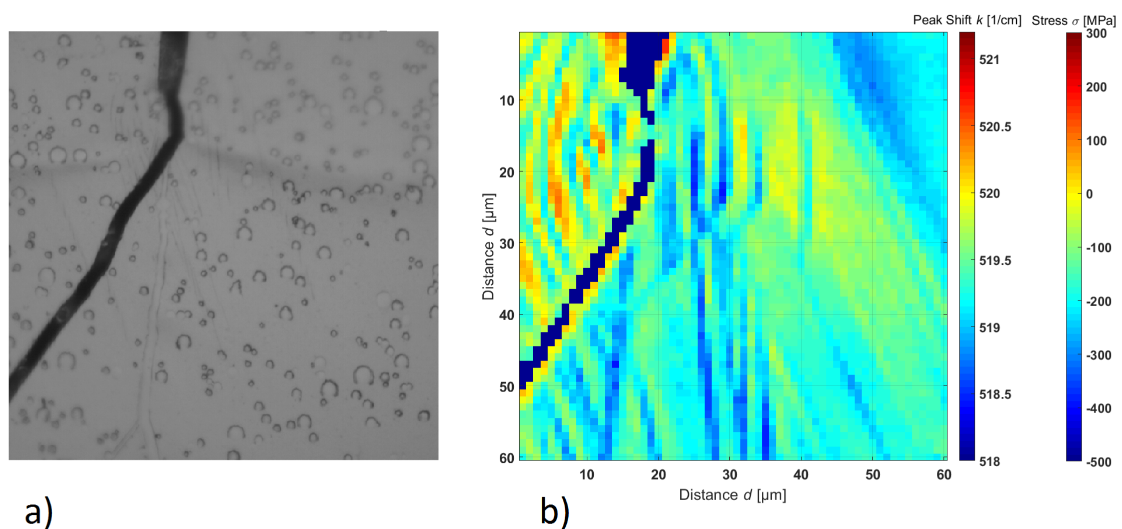

FIGURE 5.26: a) Microscopic image b) 2D map of Raman shift and stress for a cracked area form glass side. In the microscopic image, bubbles are c-Si formed during crystallization while the black area indicates the crack. In 2D map, c-Si peak is ranging between 520.5 cm^{-1} and 518.5 cm^{-1}. A tensile stress behavior up to 400 MPa is mapped on the right side of the crack. A compressive stress behavior up to 125 MPa is mapped on the left side.

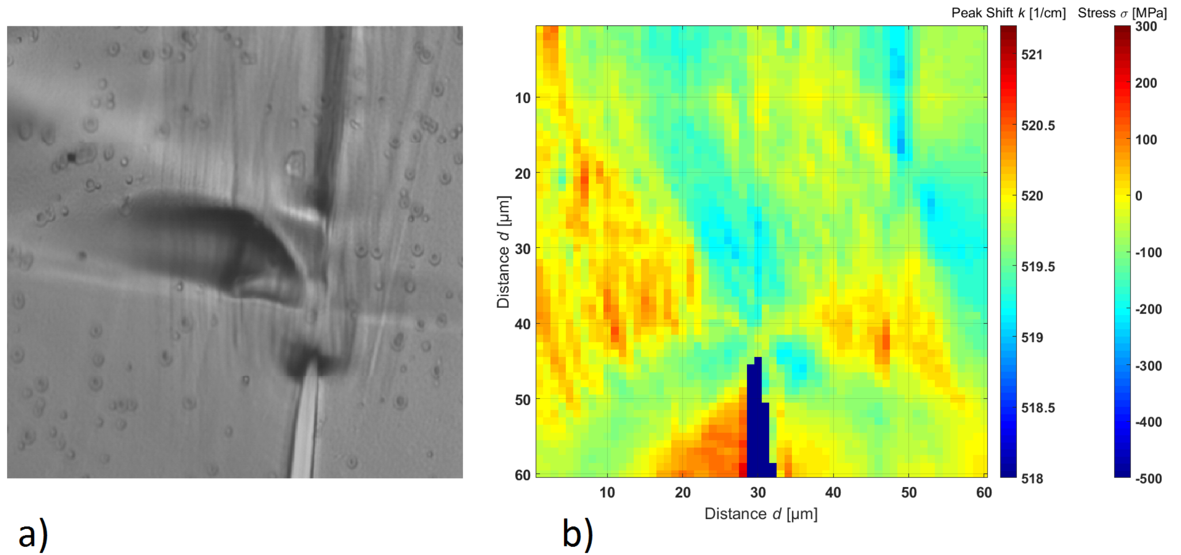

FIGURE 5.27: a) Microscopic image b) 2D map of Raman shift and stress for a crack tip form the surface side. In the microscopic image, bubbles are c-Si formed during crystallization, while the black area indicates the crack. In the 2D map, c-Si peak position is ranging between 520.8 cm^{-1} and 519 cm^{-1}. Hence a stress behavior varying between a tensile stress up to 250 MPa and a compressive stress up to 200 MPa is mapped in the same position.

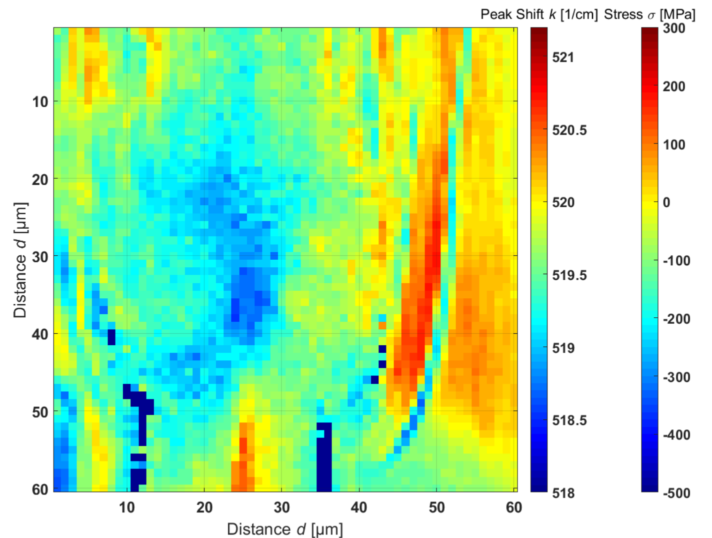

FIGURE 5.28: 2D map of Raman shift and stress for a crack tip form glass Side. The crack does not continue with depth. In the 2D map, c-Si peak position reaches a value up to 519 cm^{-1}. Hence a tensile stress behavior up to 250 MPa is mapped.

Chapter 6

Summary and Outlook

The present thesis introduces the possibility of engaging Raman spectroscopy as a characterization method with MATLAB software as the analysis tool. The analyzed data has been divided into two main categories; depth profiling as well as two dimensional mapping. Therefore, the thesis has been divided into these two categories in each chapter.

In chapter 3, the experimental steps are introduced for both sets. The first set is composed of three samples deposited on glass by plasma enhanced chemical vapour deposition with different deposition parameters. The main goal of these samples is to investigate the influence of deposition parameters (e.g.: silane concentration, rf power, and pressure) on depositing amorphous or micro-crystalline structures, as well as hydrogen content and micro-structure parameters. The first samples has a micro-crystalline structure, while the other two samples have amorphous structures. Then, the amorphous samples have been annealed from room temperature to a temperature of 510 ^{o}C for 30 minutes. The first amorphous sample shows instability in its thermal behaviour, only 10 % of total thickness has been remained on glass after annealing, and called "the unstable sample" in this thesis. While the other sample has been remained unchanged during annealing, and called "the stable sample". The main goal of this process is to investigate the influence of annealing on structural order in medium and short ranges and hydrogen diffusion. Also whether these parameters can be correlated to the thermal behaviour.

Before and after annealing and due to the low penetration depth of the blue laser on these structures, each sample has been etched by KOH to create a crater that can be used for measuring Raman spectra with depth. Then, the crater has

been measured by Dektak profilometer to have a sidewall that is good for Raman measurements (e.g.: smooth and without steeps or holes). Afterwards, the edge of the crater has been marked by a nanosecond laser to find the right orientation of the sidewall in the Raman microscope again. Finally, the measurements have been done in the single monochromatic Raman setup, by a blue laser beam of 488 nm wavelength, 200 μm length, and 1 μm width. Two Raman spectra have been measured for each point on the sidewall.

The second set is composed of five samples, which have been deposited on glass by electron beam deposition, then crystallized by liquid phase crystallization with different crystallization parameters. The main goal of these samples is to investigate the influence of crystallization parameters (e.g.: laser scan speed and power) on stress in the crystallized layers. Before measuring Raman spectra, HF dip etching has been needed to remove the capping layer on top of the LPC-Si layer. Finally, the measurements have been done in the double monochromatic Raman setup, due to its higher resolution. The same blue laser has been used, but as a spot of 1 μm in diameter.

Chapter 4 provides the detailed analysis procedure done by MATLAB software. The scripts have been modified after each scan according to the shape of Raman signal and the required evaluation of data. The first set of Raman spectra has needed a baseline fitting, combination of the two spectra to produce one spectrum for each scanned point, normalization with respect to a-Si TO mode, and fitting of each peak according to the default parameters (e.g.: peaks numbers, positions, and shapes). The integrated intensities of all peaks are then used for calculating the different properties. Finally, each property has been matched with the depth profile coming from Dektak profilometer.

The second set of Raman spectra has needed a baseline fitting, normalization with respect to c-Si peak, then peak fitting into one lorentzian peak with a variable peak position. Peak position is the only parameter used for stress calculations. Finally, the stress is exported as 2D maps, then matched with the microscopic images coming from the microscopic camera.

Chapter 5 presents and discusses the final results that have been exported for the different samples in both sets. For depth profiling, the first sample has been found to have a micro-crystalline structure. The sample has a nearly constant

crystallinity of 30 % for the first 600 nm near the surface, then it decreases gradually from 30 % to 10 % at the silicon-glass interface. While hydrogen content and micro-structure parameters are nearly constant with depth.

The two other samples have amorphous structures. For the unstable sample, MRO decreases gradually from the surface to the mid-depth, then it is nearly constant for the remaining thickness. SRO is nearly constant with depth. While for the stable sample, MRO is nearly constant for the whole thickness. SRO is also constant with depth, but with higher quantity than the unstable sample.

A comparison between depth profiles before and after annealing has been done afterwards for each sample individually. For the unstable sample before annealing, both MRO and SRO are constant with depth. While after annealing, MRO decreases gradually with depth. SRO is nearly constant for the first 400 nm but with much higher quantity than before, then decreases for the last 100 nm. For the stable sample, MRO is still constant and has a similar quantity as before annealing. SRO is still constant as well, but with slightly higher quantity than before annealing. In both samples, all of hydrogen has been diffused and the remaining is barely detected by Si-CCD detector.

In summary, Raman spectroscopy is a useful method to investigate crystallinity, structural order, hydrogen content, and micro-structure parameters in PECVD deposited precursors; hence gives a better understanding about the changes in these properties with depth. Although remarkable differences in structural order and micro-structure parameters have been noticed during the comparison, it is not yet clear if these are the control parameters for the thermal stability of the samples. However, deposition parameters of the last sample (SiH_4 flow rate of 6 sccm, H_2 flow rate of 12 sccm, pressure of 1 mbar, rf power of 25 W, and heater temperature of 450 °C) have been taken as the standard for next PECVD depositions, since they deposit an a-Si structure, that is thermally stable after annealing among all samples.

For 2D mapping, all crystallization parameters lead to successful transformation of nano-crystalline thin layers to a poly-crystalline structure. The first sample has been deformed; the capping layer has molten inside the first micrometer of the material, with no crack neither in material nor in glass. The second sample has cracks in the material only, while no cracks from glass side. The last three samples have cracks from both sides, with different number of cracks (higher laser scan

speed and power lead to higher number of cracks). Moreover, grain boundaries have been found to be increasing with increasing these parameters as well. One 2D map has been taken in a free of stress area, where peak position is found to be close to 520 cm^{-1}; hence no stress inside. Three 2D maps have been taken in grain boundaries, where peak position has been shifted to wavenumbers lower than 520 cm^{-1}.

All cracked samples have the same crack shape in the material itself. Two 2D maps have been taken in the middle of a crack, where tensile stress behavior is mapped on one side of the crack and compressive stress behavior is mapped on the other side. The last 2D maps have been taken at a crack tip. These maps show that the crack starts at the surface but does not continue with depth. A tensile stress behavior is noticed at the surface around the crack. More tensile stress is mapped near the glass. This tensile stress does not reach its threshold value to form the crack yet. The threshold values has not been not detected since the crack releases the stress.

In summary, Raman spectroscopy is a useful method to investigate the stress inside c-Si precursor layers crystallized by laser LPC for better understanding of the process. The stress inside c-Si precursors can be detected by Raman spectroscopy as a shift in c-Si TO mode away from 520 cm^{-1}. Lower wavenumbers indicate a tensile stress behavior while higher wavenumbers indicate a compressive stress behavior. In case of grain boundaries, tensile stress behavior is mainly detected and mapped. In case of cracks, stress behavior is varied between tensile stress on one side of the crack and compressive stress on the other side. LPC parameters of the first sample (red laser beam of 808 nm wavelength, substrate temperature of 510 ^{o}C, laser speed of 1 mm/s, and power of 45 W) have been taken as the standard for next LPC processes, since they produce a non-cracked layer with the minimum number of grain boundaries among all samples.

As illustrated in figure 6.1, more process need to be investigated before the fabrication of the solar cell for the industrial field. The crystallized silicon thin layer will be used as the absorber in the investigation of hetrojunction solar cells fabrication. Another approach is to increase the thickness of the precursor, to increase the efficiency and open circuit voltage.

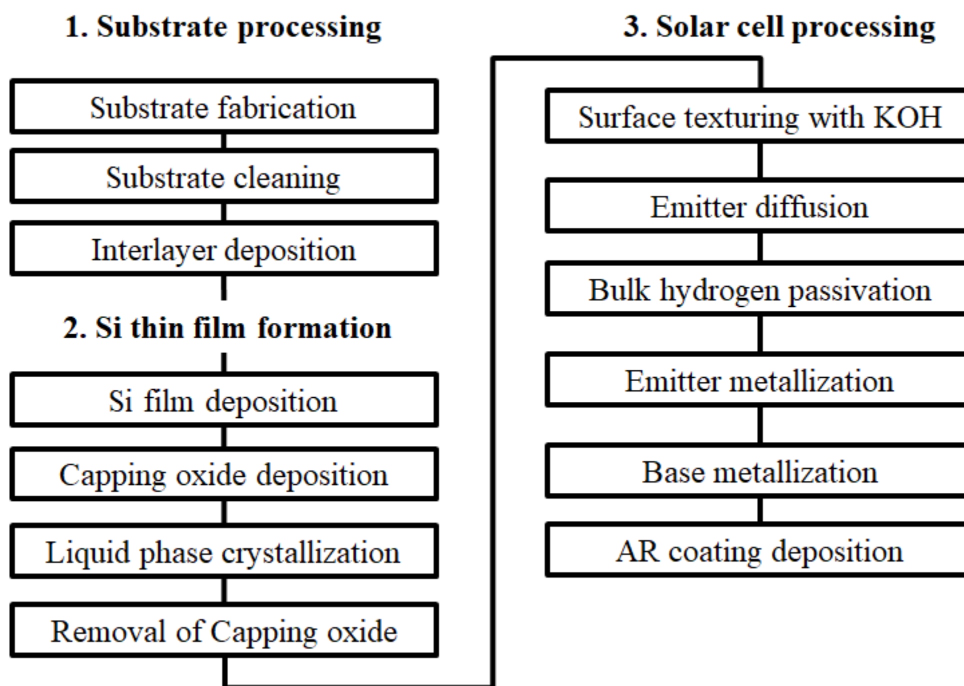

FIGURE 6.1: Process sequence of silicon thin film based solar cell fabrication.

Appendix A

An Appendix

A.1 baseline Fitting

```
function [ycorr,yfit] = newbf(y1,varargin)
def_method  = 'spline';
def_avgpts  = 3;
method = [];
avgpts = [];
pts    = [];
if isempty(method),     method = def_method;        end
if isempty(avgpts),     avgpts = def_avgpts;        end
dimy = size(y1);
lst = dimy(1);
newdimy = [dimy(1),prod(dimy(2:end))];
y1 = reshape(y1,newdimy);
x1 = 1:lst;
 x2=[x1(5),x1(62),x1(153),x1(305),x1(408),x1(505),x1(580),x1(877),x1(922),x1(988),x1(1013)];
 y2=[y1(5),y1(62),y1(153),y1(305),y1(408),y1(505),y1(580),y1(877),y1(922),y1(988),y1(1013)];

pts = round(x2.');

    npts = numel(pts);
    pss = zeros(npts,2);
    pss(:,1) = pts - floor(avgpts/2);
    pss(:,2) = pss(:,1) + avgpts;
    pss(pss < 1) = 1;
    pss(pss > lst) = lst;
    yavg = zeros([npts,newdimy(2)]);
    for n = 1:npts,
        yavg(n,:) = mean(y1(pss(n,1):pss(n,2),:),1);
    end
```

A.2 baseline Fitting

```
clear all; close all; clc
s    = dir('T:\Public\user\s.nofal\NewRaman\18j-062\*.asc'); % s is the main folder

for i=1:(length(s)/2)-30
%% IMPORTING THE 2ND PART OF THE FILES:
     filename=sprintf('18j-062_%d_2.asc',i);
     FID=fopen(filename ,'rt'); %Identify each file with an ID
     C1 = textscan(FID, '%f %f', 'Delimiter', '\t', 'CommentStyle', '#'); %Reading the data only
     fclose(FID)
     x1=C1{1}; %x-axis
     y1=C1{2}; %y-axis
%% BASELINE FITTING:
figure
[ycorr1,yfit] = newbf(y1,10);
plot(x1,y1,x1,ycorr1,'r-')
hold on
plot(x1,yfit,'-')
legend('Measured data','BesLine Model')
title(' BaseLine Fitting')
%% IMPORTING THE 1ST PART OF THE FILES:
 filename=sprintf('18j-062_%d_1.asc',i);
     FID=fopen(filename ,'rt'); %Identify each file with an ID
     C2 = textscan(FID, '%f %f', 'Delimiter', '\t', 'CommentStyle', '#'); %Reading the data only
     fclose(FID)
     x2=C2{1}; %x-axis
     y2=C2{2}; %y-axis
     ycorr2(1:711)=y2(1:711)-y2(712);
     ycorr2(712:1024)=ycorr1(1:313);
     ycorr2=ycorr2.';
     ypeak=max(ycorr2);
%% COMPINING THE 2 SPECTRAS TOGATHER:
    plot(x2,ycorr2,'b-',x1,ycorr1,'r-')
%% Gaussian Peaks Finding:
 xH=[x1(560:895)];
 yH=[ycorr1(560:895)];
 [FitResults1,FitError1]=peakfit([xH yH],0,0,2,16,0,0,0,0,[2000 2100]) %2peaks,Gaussian function
 R(i,1)=FitResults1(2,5)/(FitResults1(2,5)+FitResults1(1,5));
 %% NORMALIZATION OF H WITH Si PEAK:
 normH1(i,1)=FitResults1(1,5)/ypeak;
 normH2(i,1)=FitResults1(2,5)/ypeak;
 normsum(i,1)=normH1(i,1)+normH2(i,1);
%% 3RD WAY OF NORMALIZATION (BY YCORR OVER Y PEAK OF SILICON FROM THE 1ST PART OF THE FILES):
ynorm3=ycorr1(:)/ypeak;
D3=[x2, y3norm;x1, ynorm3];
dlmwrite(sprintf('result_%d.txt',i),D3,'delimiter','\t');
 %% Si PEAKS FINDING:
     xS1=x2(10:76);
     yS1=y3norm(10:76);
     yS1corr=yS1(1:67)-y3norm(102); % 2nd Baseline fitting
     [FitResults3,FitError3]=peakfit([xS1 yS1corr],0,0,1,16,0,0,0,140) %1peak,Gaussian function
     xS2=x2(261:316);
     yS2=y3norm(261:316); % between 1 and 0, between 480 peak and 560 minimum
     [FitResults4,FitError4]=peakfit([xS2 yS2],0,0,1,16,0,0,0,0,480) %1peak,Gaussian function
     IMRO(i,1)=(2*FitResults4(1,5))/FitResults3(1,5);
     theta(i,1)=(FitResults4(1,4)-15)/6;
end
```

A.3 Example of Depth Profiling

```
clear all; close all; clc
s    = dir('T:\Public\user\s.nofal\Berlin_samples_stress\berlin_1_1_1_surface\*.asc'); % s is the main folder
%% IMPORTING THE THE FILE:
     filename=sprintf('berlin_1_1_1_surface.xlsx');
     FID=fopen(filename ,'rt'); %Identify each file with an ID
     C1=importdata(filename)
     fclose(FID)
%% READING EACH SPECTRA ALONE:
ii=1;
for i=1:60
   for k=1:60
     x1=C1(:,1);
     y1=C1(:,ii+k);
%% BASELINE FITTING:
      [ycorr1,yfit] = newbf(y1,10);
%% NORMALIZATION (BY YCORR OVER Y PEAK OF SILICON FROM THE 1ST PART OF THE FILES):
      ypeak=max(ycorr1);
      ynorm3=ycorr1(:)/ypeak;
      D3=[x1, ynorm3];
      dlmwrite(sprintf('Result_%d_%d.txt',i,k),D3,'delimiter','\t');
   end
 ii=ii+60;
end


%% Graphic errors
opengl('save','software') % To render the graphs and prevent crash of MATLAB due to LOW-LEVEL graphics error
%close all;
```

A.4 Example of 2D mapping

```
clear all; close all; clc
s    = dir('T:\Public\user\s.nofal\Berlin_samples_stress\berlin_1_1_1_surface\*.asc'); % s is the main folder
figure
for i=1:60
    for j=1:60
      %figure
     filename=sprintf('Result_%d_%d.txt',i,j);
     FID=fopen(filename ,'rt'); %Identify each file with an ID
     C1 = textscan(FID, '%f %f', 'Delimiter', '\t', 'CommentStyle', '#'); %Reading the data only
     fclose(FID)
     x1=C1{1}; %x-axis
     y1=C1{2}; %y-axis
     xS=x1(636:657);
     yS=y1(636:657); % between 1 and 0, between 480 peak and 560 minimum
     [FitResults,FitError]=peakfit([xS yS],0,0,1,2,0,0,0,0,0,0) %1peak,Gaussian function
     error(i,j)=FitError(1,1);
     peak(i,j)=FitResults(1,2);
     FWHM(i,j)=FitResults(1,4);
     I(i,j)=max(y1);
     plot(x1,y1)
     hold on
    end
    hold on
    title('TO')
    xlabel(' \rm{Raman Shift} \it{k} \rm{[1/cm]}')
    ylabel('\rm{Normalized Raman Intensity} \it{I}\rm{_{NRA}}\rm{[r.u.]}')
end
```

Bibliography

[1] ISE Fraunhofer Institute for Solar Energy Systems. Photovoltaics report, 2018.

[2] S. Muthmann. *In-Situ Raman Spectroscopy: A Method to Study and Control the Growth of Microcrystalline Silicon for Thin-Film Solar Cells*. PhD thesis, Schriften des Forschungszentrums Jülich Reihe Energie Umwelt / Energy Environment, 2012.

[3] S. Varlamov R. Egan J. Dore, D. Ong and M. A. Green. Progress in laser-crystallized thin-film polycrystalline silicon solar cells: Intermediate layers, light trapping, and metallization. *IEEE Journal of Photovoltaics*, 4:33–39, 2014.

[4] S. Kühnapfel. *Line-Shaped Continues Wave laser crystallization of Silicon on Glass*. PhD thesis, Fakultät IV-Elektrotechnik und Informatik der Technischen Universität Berlin zur Erlangung des akademischen Grades, 2016.

[5] Helmholtz zentrum Berlin. Institute for silicon photovoltaics/helmholtz-zentrum berlin für materialien und energie, 2015, (Accessed Feb. 19, 2019).

[6] Forschungszentrum Jülich. Institute of energy and climate research iek-5 photovoltaics, 2015, (Accessed Dec. 18, 2018).

[7] Jonathan Plentz, Thomas Schmidt, Annett Gawlik, Joachim Bergmann, Gudrun Andr, Dirk Hauschild, and Vitalij Lissotschenko. Applicability of an economic diode laser emitting at 980nm for preparation of polycrystalline silicon thin film solar cells on glass. *physica status solidi (a)*, 214:1–7, 2017.

[8] Jonathon Dore, Sergey Varlamov, Rhett Evans, B Eggleston, D Ong, Oliver Kunz, Jialiang Huang, U Schubert, Kyung Kim, R Egan, and Martin Green.

Performance potential of low-defect density silicon thin-film solar cells obtained by electron beam evaporation and laser crystallization. *EPJ Photovolt.*, 4:40301(1–5), 2013.

[9] B. Rech J. Haschke, D. Amkreutz. Liquid phase crystallized silicon on glass: Technology, material quality and back contacted heterojunction solar cells. *Japanese Journal of Applied Physics*, 55, 2016.

[10] A. Jones and M. Hitchman. *Vibrational Spectra of Hydrogen in Silicon and Germanium*. 2009.

[11] T. Kieliba. *Zone-Melting Recrystallization for Crystalline Silicon Thin-Film Solar Cells*. PhD thesis, Fraunhofer Institut für Solar Energiesysteme, 2006.

[12] Nanophoton. What is raman spectroscopy, 2016, (Accessed Dec. 18, 2018).

[13] M. Nuys. *Characterization Modification of Copper and Iron Oxide Nanoparticles for Application as Absorber Material in Silicon Based Thin Film Solar Cells*. PhD thesis, Schriften des Forschungszentrums Jülich Reihe Energie Umwelt / Energy Environment, 2015.

[14] Russell S. Prago. *Physical Methods for Chemists*. Surfside Scientific Publishers, USA, 2 edition, 1992.

[15] R. Oort. *Hydrogenated Amorphous and Microcrystalline Silicon Deposited from Silane-Hydrogen Mixtures*. PhD thesis, Technische Universiteit Delft, 1989.

[16] M. Cardona. Chemical vapour deposition process and application. *Xerox Palo Alto Research Center*, 69:463–481, 1983.

[17] F. Köhler. *Zur Mikrostruktur siliziumbasierter Dünnschichten für die Photovoltaik*. PhD thesis, Schriften des Forschungszentrums Jülich Reihe Energie Umwelt / Energy Environment, 2013.

[18] S. Thapa R. Agalby and A. Gawlik. Stress and doping uniformity of laser crystallized amorphous silicon in thin film silicon solar cells. *Journal of Applied Physics*, 107:30–45, 2010.

[19] G. Andrä2 G. Sarau, M. Becker and S. Christiansen. Residual stress measurements in multicrystalline silicon bulk and thin film solar cells using micro-raman spectroscopy. *23rd European Photovoltaic Solar Energy Conference*, pages 120–132, 2008.

[20] R. Carius A. Lambertz A. Mück B. Rech O. Vetterl, F. Finger and H. Wagner. Intrinsic microcrystalline silicon: A new material for photovoltaics. *Solar Energy Materials and Solar Cells*, 62:97–108, 2000.

[21] Z. Wu H. Li C. Zhang X. Xu, H. Lin. Study of stress distribution on nanopolycrystalline silicon thin film with raman imaging spectrum, 2002.

[22] C. Maurer. *Laser Treatment of Silicon Thin-Films for Photovoltaic Applications*. PhD thesis, Schriften des Forschungszentrums Jülich Reihe Energie Umwelt / Energy Environment, 2018.

[23] S. Kurth. Raman-spektroskopische untersuchung des wasserstoffgehalts und der mikrostruktur von a-si:h präkursorschichten für flüssigphasenkristallisierte c-si solarzellen, 2018.

[24] Corning. Corning eagle xg, 2013, (Accessed Feb. 16, 2019).

[25] Wikipedia. Etching (microfabrication), 2018, (Accessed Dec. 20, 2018).

[26] Bruker. *Dektak Stylus Profiler User Manual*. Bruker Co., 2011.

[27] K. Harcha. *Principles of Vapor Deposition of Thin Films*. Elsevier Ltd., USA, 1 edition, 2005.

[28] MathWorks. peakfit-file exchange, 2018, (Accessed Feb. 22, 2019).

[29] J. Chen and D. Yang. Electron-beam-induced current study of grain boundaries in multicrystalline silicon. *Journal of Applied Physics*, 96:5490–5495, 2004.